Single Cell Transcriptomic Landscape of Diabetic Foot Ulcers

Georgios Theocharidis[#1],
Beena E. Thomas[#2],
Debasree Sarkar[#2],
William JR Pilcher[2],
Bhakti Dwivedi[3],
Teresa Sandoval-Schaefer[4],
Ruxandra F. Sîrbulescu[5],
Antonios Kafanas[6],
Ikram Mezghani[1],
Peng Wang[1],
Antonio Lobao[1],
Ioannis Vlachos[7],
Biraja Dash[8],
Henry C. Hsia[8],
Valerie Horsley[4],
Swati S. Bhasin[2],
Aristidis Veves*[1],
Manoj Bhasin*[2]

1. The Rongxiang Xu, MD, Center for Regenerative Therapeutics and Joslin-Beth Israel Deaconess Foot Center, Beth Israel Deaconess Medical Center and Harvard Medical School, Boston, MA.

2. Aflac Cancer and Blood Disorders Center, Children Healthcare of Atlanta, Department of Pediatrics and Biomedical Informatics, Emory University, Atlanta, GA

3. Winship Cancer Insitutute, Emory University, Atlanta, GA

4. Molecular, Cellular and Developmental Biology, Yale University, New Haven, CT.

5. Vaccine and Immunotherapy Center, Department of Medicine, Massachusetts General Hospital, Harvard Medical School, Boston, MA

6. Lincoln County Hospital, Northern Lincolnshire and Goole NHS Foundation Trust, UK.

7. Department of Pathology, Beth Israel Deaconess Medical Center, and Harvard Medical School, Boston, MA.

8. Yale Plastic and Reconstructive Surgery-Wound Center, Yale School of Medicine, New Haven, CT.

Equal First authors
* Co-last and corresponding authors

Corresponding authors:

Aristidis Veves, MD, DSc.
Beth Israel Deaconess Medical Center,
Palmer 321A, 1 Deaconess Rd,
Boston, MA 02215.
E-mail: aveves@bidmc.harvard.edu
Telephone: (617) 632-7075

Manoj K. Bhasin, MS, PhD.
Aflac Cancer and Blood Disorders Center
Children Healthcare of Atlanta
Woodruff Memorial Research Building, Room 4107
101 Woodruff Circle, 4th Floor East
Emory School of Medicine
Atlanta, GA 30322.
Emails: manoj.bhasin@emory.edu, mbhasin7@gatech.edu
Telephone: (404) 712-9849

Abstract

To understand the diabetic wound healing microenvironment, we profiled 174,962 single cells from foot, forearm, and PBMCs using single-cell RNA sequencing (scRNASeq) approach. Our analysis shows enrichment of a unique population of fibroblasts overexpressing *MMP1, MMP3, MMP11, HIF1A, CHI3L1*, and *TNFAIP6* genes and M1 macrophage polarization in the DFU patients with healing wounds. Further, scRNASeq of spatially separated samples from same patient and spatial transcriptomics (ST) revealed preferential localization of these healing associated fibroblasts toward deep wound/ulcer bed as compared to wound edge or non-wounded skin. ST also validated our findings of higher enrichment of M1 macrophages in healers and M2 macrophages in non-healers. Our analysis provides deep insights into the wound healing microenvironment, identifying cell types that could be critical in promoting DFU healing, and may inform novel therapeutic approaches for DFU treatment.

Introduction

Diabetic foot ulceration (DFU) is a major problem in diabetic patients as more than 15% of them are expected to develop DFUs within their lifetime. DFUs significantly impair quality of life, lead to prolonged hospitalization, and result in more than 70,000 lower extremity amputations per year in the USA alone [1]. Notably, more than half of the patients undergoing amputation due to DFU are expected to die within 5 years, a mortality rate which is higher than most cancers [2]. With the expected increase of Diabetes Mellitus (DM), DFUs will represent an even bigger burden for health systems worldwide and may prove to be one of the costliest diabetes complications [3].

Impaired wound healing leading to the development of chronic wounds in diabetic patients manifests exclusively in the foot in the presence of neuropathy and/or vascular disease [4, 5]. Various cell types, including endothelial cells, fibroblasts, keratinocytes, and immune cells play an important role in the wound healing process, but little is understood about their involvement in impaired wound healing in DFU. Dissecting cell differences within the foot ulcers between DFU patients whose ulcers are healed and those who fail to heal and go on to develop a chronic ulcer, the differences between DM patients and non-DM healthy controls, and the differences between foot with DFU and intact forearm skin in both DM and healthy subjects, along with differences in blood immune cells, can considerably increase our understanding of DFU pathogenesis/healing.

Single-cell RNA-sequencing (scRNASeq) analysis provides deep insight into cell function and disease pathophysiology by allowing the profiling of the transcriptome landscape of individual cells in heterogeneous tissues. Currently, scRNASeq is widely used in the complex biosystems of various cancers to map their microenvironment and discover molecular mechanisms and therapeutic targets [6], and concerted efforts of the human cell atlas initiative aim to fully profile all tissues of the human body [7]. Initial studies in our

groups have reported that DM and DFU patients have increased inflammatory cells and different fibroblast clusters with a distinctive injury response-associated gene expression profile, which is believed to be the result of DM related chronic inflammation [8]. Spatial transcriptomics (ST) is a more recent and novel method which enables the visualization and quantitation of the transcriptome in individual tissue sections, retaining spatial molecular information unlike scRNASeq [9].

In the present study, we primarily focused on differences between DFU patients who heal their ulcers (Healers) and DFU patients who fail to heal them (Non-healers) within 12 weeks. We hypothesize that diabetic patients with impaired wound healing have aberrant gene and protein expression profiles that leads to dysregulation of epithelial remodeling and inflammation pathways. To this end, we investigated the molecular changes via scRNASeq analysis of DFUs and forearm skin biopsies, and peripheral blood mononuclear cells (PBMCs) from patients with healing and non-healing DFUs. As control group we also performed scRNASeq analysis of the foot and forearm biopsies and PBMCs from DM patients with no DFU, and healthy non-DM patients. We also studied different sites of DFU (wound site, wound periphery, and healthy skin) to validate our findings. We finally employed immunostaining and ST on DFU sections, as well as *in vitro* experiments to confirm our most striking findings associated with DFU wound healing.

Methods

Subjects

Our study includes non-DM patients (n=10) who underwent foot surgery for various reasons, such as hallux valgus correction, as the healthy controls and DM patients without foot ulceration (n=6) who had similar foot surgery. Discarded skin specimens from the dorsum of the foot were collected for analysis. We also enrolled DM patients with plantar foot ulceration (DFU) (n=11), who underwent surgical resection of the ulcer, providing sufficient wound and peri-wound tissue for analysis. Subjects with any conditions, other than DM, or medications that could affect wound healing were excluded from the study. Four non-DM subjects, two DM patients with no DFU, and five DM patients with DFU (Healers; n=3, Non-healers; n=2) provided two 3-mm forearm skin biopsies and 20 ml of blood, from which PBMCs were isolated, within one week of the foot surgery. DFU patients were followed for 12 weeks post-surgery and were divided into two subgroups: those who healed their ulcers and those who failed to heal them (healers; n=7, non-healers; n=4). There were no major differences among the main characteristics of the studied groups (Supplementary Table 1). All patients were enrolled and followed at the Joslin-Beth Israel Deaconess Foot Center, Boston, MA, and the study was approved by the Beth Israel Deaconess Medical Center IRB (Reference number 2018P000581). For the scRNASeq analysis of spatially separated samples, multiple samples were collected

from an ischial pressure sore at the Yale Plastic and Reconstructive Surgery – Wound Center (New Haven, CT). Informed consent was obtained from all study participants.

PBMCs isolation

PBMCs were separated using Ficoll-Paque density gradient fractionation, as previously described [10], and cryopreserved in freshly prepared freezing media (90% FBS and 10% DMSO).

Single cell preparation from skin samples

Skin specimens were kept in sterile PBS on ice until processing, normally within 3h post-surgery. The skin was cleaned by sequentially immersing in 10% Betadine, 70% ethanol, and PBS for 1 min at a time. Then it was incubated in 5 mg/ml Dispase II (Thermo Fisher Scientific, 17105041) in HBSS (STEMCELL Technologies, 37150) overnight at 4°C. The next day, the epidermis was peeled off using forceps, and the tissue was finely minced with a No. 10 disposable scalpel. The skin pieces were then placed in an enzyme cocktail consisting of 3.3 mg/ml Collagenase-P (Roche, 11249002001), 3.3 mg/ml Dispase II and 1.5 mg/ml DNase I (STEMCELL Technologies, 07470) in 0.25% Trypsin-EDTA (Thermo Fisher Scientific, 25200072) and incubated for 90 min at 37°C with constant shaking, using glass pipettes for trituration every 20 min. Enzymes were then inactivated with the addition of complete DMEM (+10%FBS, +1% Pen/Strep). The single-cell suspension was passed through 70 µm and 40 µm cell strainers and centrifuged for 10 min, 500g at 4°C. For RBC lysis, ACK buffer (Lonza, 10-548E) was added. The process resulted in highly viable, typically >90%, single cell suspensions. For immediate single cell capture, the cells were re-suspended in 0.04% Ultra-Pure BSA in PBS (Thermo Fisher Scientific) and concentration was adjusted to 1000 cells/µl. If not processing for scRNASeq immediately, the cells were cryopreserved in freshly prepared freezing media (90% FBS and 10% DMSO).

Single cell RNA sequencing

The single cell preparations of the foot, forearm, and PBMC samples were used fresh or after thawing of viably frozen samples with final resuspension in PBS with 1% BSA. A droplet based ultra-high throughput scRNA-Seq system was utilized to capture single cells along with uniquely barcoded primer beads together in tiny droplets, enabling large-scale parallel single-cell gene expression studies. The gene expression (GEX) libraries were prepared using the Chromium 3'V2/3 reagent kits (10x Genomics, 120237 and 1000075). Briefly, gel bead-in-emulsions (GEMs) were generated and barcoded by loading single cell suspensions along with gel beads and reverse transcription (RT) master mix in 10x Genomics Single cell chip (A chip kit,120236; B chip kit, 1000153) and running on the chromium controller (10x Genomics, 110211). Following RT, the cDNA was amplified and used to generate 3' GEX libraries. The cDNA and GEX libraries were

quantified using Qubit 3.0 fluorometer (Life technologies, 15387293), and quality was assessed using HS DNA chips (Agilent technologies, 5067-4627) with 2100 Bioanalyzer (Agilent technologies, G2939BA). Sequencing was performed using massively parallel sequencing on the Novaseq S4 platform (Illumina). We produced ~40,000 - 50,000 reads per cell capturing the expression of ~1,000 - 2,000 transcripts per cell.

Data processing and analysis

Raw scRNASeq data was demultiplexed, aligned to the reference human genome (Hg38), and processed for single cell gene counting using the Cell Ranger Software from 10X Genomics Inc. The single cell count data was normalized using the SCTransform algorithm in Seurat v3.0 Bioconductor package [11] that uses regularized negative binomial models for normalizing sparse single cell data. The normalized expression profiles of the samples were merged, and undergone quality control, pre-processing, unsupervised and supervised analysis using various R and Bioconductor packages. The quality filtering on scRNASeq data was performed by multiple filtering parameters including: >50% of mitochondrial genes, cells expressing the lower number of genes (< 200 genes), and genes only uniquely expressed in < 3 cells.

The unsupervised analysis using principal component analysis (PCA) was performed on variable genes to identify principal components which captured the most variance across the samples. These principal components were used as an input for Uniform Manifold Approximation and Projection (UMAP) analysis [12] to determine the overall relationship among the cells. Cells with similar transcriptome profiles clustered together, and the clusters were subsequently annotated to different cell types based on the expression of specific well established cell marker transcripts. Comparative analysis of the single cell landscape of healing and non-healing DFUs, along with healthy non-DM subjects and non-DFU DM patients as controls, was performed using split UMAP plots, for determining heterogeneity (based on clusters of cells) and abundance of cell types. The significance testing change in abundance of cell types across clinical groups was performed either using one-way ANOVA or Welch's t-test (p-value <.05). Similar analysis was also performed for the 3 different anatomical sites separately from where the samples were collected, i.e., foot, forearm, and peripheral blood. To further characterize cell type specific differences among clinical groups, we performed comparative analyses using multiple tests corrected non-parametric Wilcoxon Rank Sum test (P Adjusted value=0.01, Fold Change=1.2) on individual cell types like fibroblasts, keratinocytes, T-lymphocytes, natural killer cells, monocytes, macrophages, mast cells, B-lymphocytes, plasma cells and dendritic cells.

Pathways and Systems Biology analysis

To precisely characterize the cell types and understand the molecular mechanism of wound healing, we performed pathways enrichment and systems biology analysis. The

analysis was performed on transcripts that were significantly dysregulated in the specific cells by comparing healed vs non-healed samples. Pathways and systems biology analysis was performed using the Ingenuity Pathway Analysis software package (IPA 9.0) (Qiagen). A detailed description of IPA is available at the Ingenuity Systems' website (http//www.ingenuity.com). Systems biology analysis was performed by analyzing the upstream transcriptional regulators. The regulatory analysis helps in identifying significantly activated or inhibited transcriptional regulators based on upregulation or downregulation of its target genes. The significance of transcriptional regulators activation/inhibition was determined using one-tailed Fisher 's exact test. The regulators with a p-value <.01 and absolute z-score 2 were considered statistically significant.

Ligand and receptor-based Cell Interaction analysis

NicheNetR [13] was used to identify ligands produced by healer-specific fibroblasts which could uniquely regulate other healer-specific fibroblasts. NicheNetR uses a prior model of ligand-target interactions derived from a meta-analysis of multiple sources to identify ligands which may explain expression differences in a given gene set. In this workflow, cells are classified as either senders or receivers. The expression of sender cells is used to identify possible ligands, while the receiver cells are used to generate a gene set. In this case, Cluster 3 with overexpression of *MMP1, MMP3, CHI3L1, CCL20*, and *TIMP1* from the healer-specific fibroblasts was treated as a sender cluster, while other healer-specific clusters (Fig. 5; clusters 4, 6, 13) or non-specific clusters (Fig. 5; 0, 2, 5) were treated as receivers. The gene sets used were the markers differentially expressed between DFU-healers specific clusters and non-specific clusters within the receiver subsets. The top markers are combined with NicheNetR's ligand-target weights to compute the Pearson correlation coefficient between ligands and expression changes in the receiver subset. A high Pearson correlation coefficient between ligand and target gene set indicate that expression of ligand might be responsible for expression differences. For a ligand to be considered for interaction analysis, it must be expressed in at least 5% of the sender cell population, and its corresponding receptor must be expressed in 5% of the receiver cell population.

Immunofluorescence staining and imaging

5 µm thick frozen sections from healing and non-healing DFUs were fixed in 80% ice cold acetone for 10 min, blocked with 5% donkey serum in 0.2% PBS-Tween for 30 min at room temperature and incubated overnight in a humidified chamber at 4°C with primary antibodies: mouse monoclonal anti-FAP (1:50, clone F11-24, sc-65398, Santa Cruz Biotechnologies), rabbit polyclonal anti-CHI3L1 (1:100, ab77528, Abcam) and goat polyclonal anti-TIMP1 (1:100, AF970, R&D Systems). Alexa Fluor donkey anti-rabbit 488-, anti-mouse 594- and anti-goat 647-conjugated secondary antibodies (1:1,000, 1:500 and 1:1,000 respectively, all Abcam) were added the next day for 1 hour at room temperature. DAPI was included for nuclear counterstaining. TrueVIEW

Autofluorescence Quenching Kit (Vector Labs, SP-8400) treatment was employed to enhance staining. Tissue sections were mounted in ProLong Gold Antifade (Thermo Fisher Scientific, P36930) and visualized with a Zeiss LSM 880 (Carl Zeiss) inverted confocal microscope and images processed with ZEN 2011 (Carl Zeiss) and ImageJ/FIJI (NIH) software packages.

Spatial transcriptomics

The spatial transcriptome profiling was performed using NanoString's GeoMx Digital Spatial profiling platform on unfixed frozen 5 µm tissue sections. Samples were processed as follows: 1) 10% neutral buffered formalin (NBF) fixation overnight, 2) target retrieval (1X Tris EDTA, pH 9.0 for 20 min), 3) proteinase K digestion (1 µg/mL for 15 min), 4) post-fixation (10% NBF, Tris-glycine stop buffer), 5) in-situ hybridization overnight with the GeoMx Cancer Transcriptome Atlas probe panel (1800-plex), 6) stringent washes (50:50 formamide/4X SSC), and 7) fluorescent antibody/marker (aSMA, Clone: 1A4, Abcam; CD45, Clone: 2B11+PD7/26, Novus; PanCK, Clone: AE1/AE3, Novus) incubation, 1 h at room temperature. Sections were then loaded onto the GeoMx® Digital Spatial Profiler (Nanostring, GMX-DSP). For profiling, circular regions of interest (ROIs), approximately 500 µm in diameter, located within the ulcers or in neighbouring non-ulcerated tissue were selected to include high concentrations of CD45+ immune cells in close proximity to vessels (αSMA+ structures). After ROI selection, the GeoMx instrument illuminated each ROI separately with UV light to cleave, aspirate, and deposit the oligonucleotides from the hybridized ISH probes for downstream sequencing into a 96-well plate. Library preparation (PCR, AMPure bead purification) was performed, followed by paired-end sequencing with an Illumina NextSeq 550. Sequencing data (FASTQs) was then processed with a custom GeoMx NGS pipeline (DCCs) to be analysed in part with the GeoMx Data Analysis Suite. Raw reads were processed for high quality with TrimGalore and FLASH [14]. Reads were then aligned to analyte barcode with Bowtie2 [15]. PCR duplicates were discarded using UMI-tools with the Hamming distance set at three. Poorly performing probes were removed from analysis if they were outliers (Grubbs test) or had low counts relative to other probes targeting the same gene. Raw probe count data (up to 5 unique probes per gene) were condensed into gene level count data and normalized with the quartile 3 gene count value per ROI individually. Complete-linkage hierarchical clustering was performed on normalized counts and represented by heatmap using the R function pheatmap. Unpaired t-test with Benjamini-Hochberg procedure for adjusted p-values was used to calculate differentially expressed genes with a threshold $p<0.05$. Significantly expressed genes were entered on Metascape (Version 3.5, http://metascape.org) for enrichment analysis with Gene Ontology (GO) Biological Processes (Version 2020-09-16). All genes in the human genome were used as the enrichment background. P-values were calculated based on cumulative hypergeometric distribution and Q-values were calculated using the Benjamini-Hochberg procedure for multiple testing. A term was considered overrepresented when $p<0.01$, had a minimum

count of 3 and an enrichment factor >1.5, which is the ratio between the observed counts and the counts expected by chance.

Cell culture

Normal human dermal fibroblast cells (BJ CRL-2522) were obtained from ATCC and maintained in Eagle's minimum essential medium (EMEM) (ATCC, 30-2003), supplemented with 1% (v/v) penicillin/streptomycin (P/S) and 10% (v/v) fetal bovine serum (FBS) (Sigma-Aldrich, F1435). For passaging, cells at ~80% confluence were detached through a 5- to 10-min incubation with 0.05% Trypsin/EDTA and further resuspended in complete EMEM. Cells were then centrifuged at 1,200 rpm for 5 min. The cells were replated at a concentration of 6,000 cells/cm^2 and/or cryopreserved with 90% FBS and 10% DMSO freezing media. Cells were maintained in 95% O_2, 5% CO_2 at 37°C and routinely tested for mycoplasma contamination (PromoKine, PK-CA91-1096).

Transduction of fibroblasts with Precision LentiORF viral vectors

Cells were seeded in 6-well culture plate at 150,000 cells per well and pre-incubated with 5 µg/ml polybrene for 10 min at 37 °C. Afterwards, cells were incubated overnight with culture medium containing 5 µg/ml polybrene and the viral particles carrying the *CHI3L1* gene (OHS5899-202624268, Horizon Discoveries) or the positive control viral particles (OHS5833) at a multiplicity of infection of 10. After removal of the particles containing medium, cells were incubated in culture medium with 10 µg/ml Blasticidin to positively select transduced cells. Transduction efficiency was evaluated with assessment of GFP expression, for both target and control constructs and RFP expression, for the control construct, on a K2 Cellometer (Nexcelom Bioscience) and with live cell imaging on a Zeiss LSM 880 microscope.

Real time qPCR

RNA was extracted from 100,000 cells using the miRNeasy Mini Kit (Qiagen, 217004). RNA quantification was done by using the Qubit RNA BR Assay kit (Cat. No. Q10210) and the Qubit 3 Fluorometer. cDNA was used at a concentration of 15 ng/ml from 1 µg of RNA and reverse transcribed with the miScript II RT kit (Cat No. 218161). RT qPCR analysis was run for the samples using a miScript SYBR Green PCR Kit (Cat. No. 218073) on a Stratagene Mx3005P (Agilent Technologies). Housekeeping gene *GAPDH* primers were purchased from Qiagen (Cat. No. QT00079247) and *CHI3L1* primers, were obtained from MGH-HMS primer bank with the following sequences: FW: 5'-GAA GAC TCT CTT GTC TGT CGG A-3' and RV: 5'-AAT GGC GGT ACT GAC TTG ATG-3'. Data were normalized to the expression of *GAPDH* and were analyzed using the $2^{-\Delta\Delta CT}$ method.

Western blotting

500,000 cells were centrifuged at 130xg for 5 min at 4 °C, washed with ice-cold PBS, and centrifuged again at 2,400xg for 5 min at 4 °C. The pellet was then resuspended in ice-

cold RIPA buffer (Prod# 89901) supplemented with 10 µl/ml protease and phosphatase inhibitors (Prod# 78430 and 78420) and incubated for 15 min on ice with periodical pipetting and vortexing. Samples were then centrifuged at 14,000xg for 15 min at 4 °C and supernatants were collected. Protein concentration was measured using the Pierce™ BCA Protein Assay Kit (Cat. No. 23225). The protein samples were reduced by using a 6x Laemmli buffer, and boiled at 95°C for 5 min. 30 µg of protein per sample was loaded into 12% SDS-PAGE gels and run at a constant 200 V for 40 min. The gel was washed with Tris-buffered saline-Tween 20 (TBST), and incubated in blotting buffer for 10 min. The transfer ran overnight in a cold room at a constant 90 mA. Once transfer was complete, the blot was washed in TBST, and blocked with 5% BSA for 1 h at room temperature. Blot was then incubated in 5% BSA with CHI3L1 (Abcam, ab77528 1:1,000) or GAPDH (ab9485, 1:5000) antibodies for 1 h at room temperature. Afterwards, the blot was washed in TBST, and incubated with a secondary antibody (ab205718 1:10,000) for 1 h at room temperature. Finally, a chemiluminescent substrate (Cat. #1705062) was added and the blot was visualized using the ChemiDocTM Touch Imaging System (Bio-Rad). For stripping, the blot was washed in TBST and incubated in stripping buffer (Prod# 46430) for 45 min at room temperature. After stripping, the blot was washed with TBST, blocked with 5% BSA for 1 h at room temperature and reprobed as previously described.

Adhesion assay

Transduced BJ cells were plated at 50,000 cells per well in 12-well plates pre-coated with 10 µg/ml human fibronectin (Prod# 33016-015) and incubated for 1 h at 37 °C. Afterwards, cells were washed with PBS, fixed with 4% paraformaldehyde for 15 min, and stained with 0.05% crystal violet for 30 min at room temperature. Pictures of the adherent cells were taken on a Primo Vert inverted microscope (Carl Zeiss) with an Axiocam 105 camera. Pictures of two random fields were taken per well, for at least three wells per condition, and cells were counted using ImageJ/FIJI software. Three independent experiments were performed.

Scratch assay

Transduced BJ cells were plated at 50,000 cells per well in 24-well plates. The cell monolayer was scratched in a straight line using a 200 µl pipette tip. Debris were removed by washing once with media, then cells were incubated in medium supplemented with 5% FBS throughout the experiment. Images were taken immediately after the scratch, in 6 h, and in 12 h for four wells per condition. Scratch areas were analyzed using ImageJ/FIJI. Three independent experiments were performed.

Data availability

Spatial transcriptomics and scRNASeq data have been submitted to NCBI's Gene Expression Omnibus (GEO) and are accessible through GEO accession numbers GSE166120 and GSE165816. An interactive data resource and analytical tool developed

based on this DFU single cell data is available online at https://bhasinlab.bmi.emory.edu/Diacomp.

Results:

DFU healing is significantly associated with a subset of fibroblasts

To identify local and systemic factors associated with DFU healing, we examined the cellular landscape of DFUs by scRNASeq analysis of skin specimens from DFU, foot, forearm, and PBMC samples. We analyzed 54 samples from 17 diabetic patients (11 with and 6 without DFU) and 10 healthy non-DM subjects. The study cohort, objectives, and analysis strategy are outlined in Fig. 1a. In total, we sequenced 174,962 cells (94,325 from foot, 37,182 from the forearm, and 43,455 from PBMC samples) and created a genes expression matrix for each cell, which we used to perform dimensionality reduction by UMAP and graph-based clustering, thereby identifying 37 orthogonal clusters of cells. The expression of established cell-specific marker genes assisted in the annotation of these 37 cell clusters into 21 distinct cell types (Fig. 1b, c). We identified most of canonical cell types observed in the human skin [16, 17] and PBMCs [18], namely: smooth muscle cells, SMCs (*TAGLN*$^+$*, ACTA2*$^+$); fibroblasts, Fibro (*DCN*$^+$*, CFD*$^+$); vascular endothelial cells, VasEndo (*ACKR1*$^+$); T-lymphocytes, T-lympho (*CD3D*$^+$); CD14$^+$ monocytes, CD14-Mono (CD14$^+$*, S100A9*$^+$); differentiated keratinocytes, DiffKera (*KRT1+, KRT10*$^+$); basal keratinocytes, BasalKera (*KRT5*$^+$*, KRT14*$^+$); natural killer cells, NK (*CCL5*$^+$*, GZMB*$^+$); NK and T cells, NKT (*CD3D*$^+$, *CCL5*$^+$); CD16$^+$ monocytes, CD16-Mono (*FCGR3A*$^+$*/CD16*$^+$); M1 macrophages, M1-Macro (*IL1B*$^+$); M2 macrophages, M2-Macro (*CD163*$^+$); melanocytes and Schwann, Melano/Schwann (*MLANA*$^+$*, CDH19*$^+$); sweat and sebaceous gland cells, Sweat/Seba (*DCD*$^+$); lymphatic endothelial cells, LymphEndo (*CCL21*$^+$), erythrocytes, Erythro (*HBB*$^+$); dendritic/Langerhans cells, DCs (*GZMB*$^+$, *IRF8*$^+$); B-lymphocytes, B-lympho (CD79A$^+$, *MS4A1*$^+$); plasma cells, Plasma (*MZB1*$^+$), and mast cells, Mast (*TPSAB1*$^+$) (Fig. 1c). Comparative analysis of cell type abundance revealed substantial variations in the enrichment across clinical groups (Fig. 1d). Interestingly, our analysis showed significant heterogeneity in the transcriptome profile of fibroblasts and identified a unique population of fibroblasts that are over-represented in the samples from DFU-healers (Fig 1b, d). We will refer to these as **H**ealing **E**nriched - **Fibro**blasts "HE-Fibro" in the rest of the article. Further, the gene signature for each cell cluster was defined by comparing the expression profile of the target cluster with the rest of cells based on non-parametric Wilcoxon Rank Sum test (P-value <0.01 and Fold Change >2) (Fig. 1e). In-depth analysis of the HE-Fibro cell cluster revealed high expression of multiple extracellular matrix (ECM) remodeling (*MMP1, MMP3*) and immune/inflammation (*CHI3L1, TNFAIP6*) associated genes (Fig. 1f). MMP1 (Matrix metalloproteinase-1) [19] interacts with CD49b [20], an integrin alpha subunit involved in cell adhesion and cell-surface-mediated signaling in T, NK, and NKT cells [21], fibroblasts, and platelets.

CHI3L1 (Chitinase-3-like protein 1) is a secreted glycoprotein that has been previously associated with pathogenic processes related to inflammation and ECM remodeling [22]. TNFAIP6 (Tumor necrosis factor Alpha Induced Protein) is known to be involved in ECM stability and cell migration, and its expression is correlated with proteoglycan synthesis and aggregation [23]. This protein has shown anti-inflammatory effects in various models of inflammation, which suggest that it is a component of a negative feedback loop capable of downregulating the inflammatory response [24]. The distinct and previously undescribed subtype or state of fibroblasts, HE-Fibro, with overexpression of matrix remodeling, immune and inflammatory genes, may contribute to successful wound repair in DFU healers. The top 10 overexpressed genes from the annotated cell clusters are included in Supplementary Table 2.

Exploring cellular heterogeneity across different anatomical sites

To assess tissue specific cellular heterogeneity along with gene expression and molecular pathway alterations, we generated the UMAP rendering spilt based on foot, forearm, or PBMC samples (Fig. 2a). The analysis depicted significant variations in the abundance of cell types based on anatomical sites (Fig. 2b). Fibroblasts, smooth muscle cells, melanocytes, sweat gland cells, vascular and lymphatic endothelial cells were enriched in the foot samples. The analysis on keratinocytes revealed a predominance of basal and differentiated keratinocytes in the foot and forearm samples respectively (Fig. 2a, b). Interestingly, 99.94±1.58% (mean ± stderr) of HE-Fibro cells, were identified in the foot samples (Fig. 2a, b, supplementary table 3), indicating that these are foot specific cells. The analysis demonstrated that a significant fraction of immune cells was contributed by the PBMC samples. $CD14^+$ (98.47±1.06%) and $CD16^+$ (99.63±1.11%) monocytes were observed predominantly in the PBMC samples. Dendritic, NK and NKT cell populations were also predominantly present in PBMC samples. The highest abundance of M2 macrophages (71.28±1.27%) and mast cells (82.51±1.49%) was observed in the foot samples, with lower proportions in the forearm samples, and lowest in the PBMCs. On the adaptive immune system side, 31.27±0.27% of T-lymphocytes came from the foot samples, 12.42±0.35% from the forearm, and the remaining 56.31 ±1.21% from the PBMCs (Fig. 2b, supplementary Table 3). In contrast, more than half of plasma cells were derived from foot (66.01±1.89%), and the remaining were almost equally proportioned between forearm and PBMCs. Most of the B-lymphocytes (84.49 ±1.63%) originated from PBMCs.

To more closely examine the gene expression landscape of cells with differential abundances between foot and forearm i.e., fibroblasts and keratinocytes, we performed comparative analysis on their transcriptome profiles (Fig 2 c-f). The foot fibroblasts exhibited upregulation of multiple molecules associated with ECM remodeling and immune response. This may be attributed to the enrichment of HE-Fibro population in the foot samples (Fig 2c). Genes that were overexpressed in foot fibroblasts include gene for

Wnt signaling antagonist, secreted frizzled-related protein 4 (*SFRP4*) and genes directly related to ECM organization, asporin (*ASPN*) and tenascin C (*TNC*). Wnt signaling is crucial for effective wound healing [25, 26] and its modulation is closely linked with TGFβ expression [27] , which is in line with the enhanced expression of *TGFB1* in these fibroblasts. Tenascin C is known to upregulate TGFB1 as well as promote expression of type I collagen in fibroblasts, which is essential for maintaining ECM integrity [27]. The cellular development (*TSPAN8, WIF1*) and immune cell trafficking (*CCL19*) related genes were significantly overexpressed in the fibroblasts from the forearm (Fig. 2c). Pathway analysis on fibroblast differentially expressed genes (DEGs) revealed significant (P value < .01) activation of ILK, leukocyte extravasation signaling, RhoA signaling, and actin cytoskeleton signaling in the fibroblasts from the foot samples (Fig. 2d). The comparative analysis between foot and forearm keratinocytes showed significant upregulation of basal (*KRT6A, KRT16, KRT17*) and differentiated (*KRT2*, *KRT10)* keratinocyte associated genes in the foot and forearm samples, respectively. This discrepancy can be explained by the fact that forearm biopsies represent unwounded tissues with fully stratified epidermis, as opposed to foot samples that include DFUs with partially formed epithelium, and therefore fewer differentiated keratinocytes. Moreover, the differences between plantar glabrous skin and forearm hairy skin could contribute to the disparity [28]. In addition to upregulation of alarmins like *KRT6A*/*16*/*17* at the wound site [29], we also observed upregulation of inflammatory molecules including *S100A8* and *S100A9*, known to activate the immune system in response to skin injury [30]. Further pathway analysis on foot keratinocyte DEGs uncovered significant activation of immune and inflammatory pathways including ILK and IL-8 signaling (Fig. 2f).

Systemic dysregulations revealed by comparative analyses of PBMCs across clinical groups

To better understand the impact of DFU at a systemic level, we performed separate analysis on PBMC samples alone from 4 clinical groups, viz “Healthy” (healthy subjects without DM), “DFU-Healer” (DM patients with healing DFUs), “DFU-Non-healer” (DM patients with non-healing DFUs), and “Diabetic” (DM patients without DFU) (Fig. 3a). The cell annotation was done using well established marker genes (supplementary material 1). The DFU-Healers were observed to have higher proportions of naïve and early differentiated progenitor T-lymphocytes, T-lympho, expressing *CCR7*, shown to have a role in activation of various T cell subsets [31] (Fig. 3b). On the other hand, DFU-Non-healers had a higher proportion of cytotoxic NKT cells (*IL7R, GZMB, KLRD1*), indicating a shift in T-cell subpopulations correlating with DFU healing (Supplementary material 2). We observed statistically significant higher *CCR7*+ T-lympho cells to NKT cells ratio (P value <.01) in the DFU-Healers as compared to DFU-Non-healers and DM patients without DFU, indicating the association of these T-cells with successful wound healing (Fig. 3b). A significantly higher proportion of *CCR7*+ *CD8*+ T cells (cluster CD8T2 in Figure 3a) was also observed in DFU-Healers as compared to DFU-Non-healers (Fig.

3c). Further DEGs analysis on these T-lympho, CD8T2 and NKT cells indicated overexpression of T-cell specific genes like *IL7R*, *TCF7*, and *CCR7* in the DFU-Healers, whereas DFU-Non-healers overexpressed NKT lineage genes like *NKG7*, *GNLY*, *CCL5,* and *KLRD1* (Fig. 3c). Pathways analysis on these T/NKT cells DEGs demonstrated inhibition of key immune and inflammation pathways including IL-6, IL-8, CD28 Signaling in T helper cells, and iCOS-iCOSL pathways and activation of RhoGDI and EIF2 signaling in the DFU-Healers, as compared to DFU-Non-healers at systemic level (Fig. 3d). Further systems biology analysis revealed inhibition of several upstream regulators of immune pathways including *CD44*, *TGFB1*, *CCL5*, and *NFKBIA* in the T cells from PBMCs of patients with healing DFUs (Fig. 3e). This was in accordance with the observed reduced gene expression of *NFKBIA, CCL5* and *TGFB1* in DFU-Healers compared to high expression in DFU-Non-healers (Fig. 3f). In aggregate, these results underscore the enrichment of naïve T cells with a prevalence of immune inhibitory pathways and processes for DFU-Healers, and a state of chronic inflammation for DFU-Non-healers, at the systemic level.

T, NK and NKT cells exhibit distinct cell subpopulations in DFU-Healers and DFU-Non-healers

The focused sub-clustering analysis on the T, NK and NKT cell populations identified 17 subclusters (Fig. S1a). *CD4*+ (subclusters 0, 4, 10) and *CD8*+ (subcluster 14) naïve T cells (*CCR7*$^{+}$*, LEF1*$^{+}$), that can self-renew and proliferate readily into other T cells, were enriched in DFU-Healers (Fig. S1b, c; Supplementary material 3 c, d). Cluster 6, CD8^{+} effector T cells (*CCL5*$^{+}$*, GZMB*$^{+}$*, IL32*$^{+}$*, GZMK*$^{+}$), enriched in DFU-Healers, also expressed higher levels of *CD27, a* key molecule in generation and maintenance of T cell immunity [32].

NKT (*CD8*$^{+}$*, CCL5*$^{+}$*, GZMB*$^{+}$*, IL32*$^{+}$*, GZMH*$^{+}$) cells subclusters 5 and 7 were enriched in Diabetic and DFU-Non-healer groups respectively (Fig. S1a, b; Supplementary material 3 c,d). The DFU-Non-healer enriched subcluster 7 also had high expression of T cell exhaustion marker, *TIGIT* (Supplementary material 3 d). Sample site specific split t-SNE plots revealed separate clustering of T, NK/T and NK cells from skin and PBMC (Supplementary material 3 a). Subclusters 1,2,9,11 and 13, expressing activation markers *CD69* and CD*44*, were largely made up of skin samples derived from foot (Supplementary material 3 b-d). Clusters 1 and 9 were positive for T cell exhaustion markers (*TIGIT*$^{+}$*, HAVCR2*$^{+}$*, LAG2*$^{+}$) (supplementary material 3c). In PBMCs, DFU-Healers appeared to have more nonpolarized central memory and naïve T-cells (Fig S1b, c, supplementary material 3). *CD27* (supplementary material 3c), which characterizes central memory T-cells that lack immediate cytotoxicity [33], was also more in the DFU-Healers. In contrast, DFU-Non-healers were enriched with cytotoxic NKT cells (cluster 7), expressing *GZMH*, *GZMA* and *GZMB* (Fig. S1b, supplementary material 3c). These granzyme molecules have been previously implicated in impaired wound healing development by promoting

chronic inflammation, vascular dysfunction, and reduced cell adhesion [34]. We also observed a unique $CD4^+$ cluster (cluster 10, Fig. S1a) that was predominantly present in DFU-Non-healers and enriched for *GIMAP1* and *GIMAP4*, both shown to be implicated in T helper cell differentiation towards the Th1 lineage [35]. In the Diabetic group, a *GZMH*$^+$*, GNLY*$^+$ and *CCL5*$^+$ expressing cluster (cluster 5) was prominent, pointing toward the presence of specialized DM associated NKT cells. CCL5 or RANTES, a potent chemoattractant of immune cells, has been reported to be strongly downregulated in DFUs compared to acute wounds, and could represent a potential therapeutic target [36]. In summary, while skin samples derived T/NKT cells did not show significant differences between DFU-Healers and DFU-Non-healers, potentially due to the low number of recovered T cells, a definitive enhancement of naïve T cells was seen in PBMCs of DFU-Healers compared to more cytotoxic NKT cells in DFU-Non-healers.

Analysis of foot ulcer cells reveals the significance of localized inflammation in diabetic wound healing

To map the transcriptome and cellular landscape of the site for DFUs, we performed focused analysis on single cell profile of 94,325 cells from 26 foot samples. Split UMAP analysis indicated differential abundance of cell types among the four clinical groups (Fig 4a, Supplementary material 4). The DFU-Healers had a significantly higher number of HE-Fibro cells (P value <.05) as compared to DFU-Non-healers, Diabetic patients and non-DM healthy controls (Fig 4b). Additionally, the DFU-Healer group also showed a significantly higher proportion of M1 macrophages (classically activated macrophages that promote inflammation) than M2 macrophages (alternatively activated macrophages with anti-inflammatory properties), as opposed to DFU-Non-healers (Fig. 4c). Also, a group of SMCs, SMC2, with overexpression of proliferation markers *CENPF, PTTG1, MKI67* and*TOP2A* was significantly enriched in DFU-Healers (Fig. 4d, supplementary table 4), highlighting the presence of a highly proliferative SMC cluster in healing DFUs. Other cell types also exhibited variation across clinical groups but did not achieve statistical significance due to intragroup variation among patients (Fig. 4e). DEGs analysis on DFU-Healers vs. Non-healers and M1 macrophages vs. M2 macrophages identified a signature comprising of 195 genes that were differentially expressed in M1 macrophages from DFU-Healers (Fig 4f). DFU-Healer enriched macrophages overexpressed inflammatory genes including *IL1B, S100A8*, and *S100A9* to mount an acute inflammatory response for promoting wound healing. On the other hand, DFU-Non-healer macrophages overexpressed genes from the complement system like *C1QA/B/C*, which are associated with M2 macrophage like anti-inflammatory responses [37] (Fig 4f). Pathway analysis showed activation of the IL-17 signaling pathway, a known regulator of inflammatory response [38], in DFU-Healers (Fig. 4g). The upstream regulators activated in DFU-Healers included HIF1A, TNF, STAT5a/b, TLR7, TLR9 and IL17R/C (Fig. 4h), whereas SOX4, TGFB1, and NANOG, were inhibited (Fig. 4i).

Similar analyses were also conducted on the forearm cells (Fig S2a, supplementary material 5). Differentiated keratinocytes were enriched in DFU-Healers compared to DFU-Non-healers (Fig S2b). We found that LGALS7 or Galectin-7, which has been previously implicated in keratinocyte migration during re-epithelialization of wounded epidermis [39], is the top differentially expressed gene in the forearm keratinocytes of DFU-Healers (Fig S2c).

Healing associated fibroblasts drive DFU healing by promoting matrix remodeling and inflammatory response

To further delineate the role of fibroblasts in wound healing, we performed focused analysis on fibroblasts that produced 14 subclusters, representing different molecular states or subtypes of fibroblasts (Fig. 5a). The majority of subclusters showed distinct expression profiles indicating heterogeneity in the fibroblast population (Fig 5b). Subclusters 0, 1, 2 and 5 comprised most of the cells from unwounded skin. Subcluster 0 was characterized by the expression of reticular fibroblast marker *MGP* [40] and multiple adipocyte associated genes (*APOE*, *APOD*, *CFD*), consistent with the enhanced adipogenic potential of these cells [41]. Subclusters 2 and 5 contained cells expressing papillary fibroblast markers *PTGDS*, *APCDD1* and *COL23A1* [42, 43], while subcluster 1 was enriched for *WISP2*, *PI16*, *SLPI* and *SFRP2* which describe fibroblasts residing both in the papillary and reticular dermis and are believed to contribute to ECM homeostasis [44-46]. The evaluation of cellular makeup of clusters unveiled a higher proportion of cells (58% - 90%) from DFU-Healers in specific subclusters; clusters 3, 4, 6 and 13. These four sub-clusters represent four heterogeneous states or subtypes of the HE-Fibro (Fig 5a, marked area). Further generation of gene signatures for these subclusters revealed that cluster 3 was significantly enriched with cells expressing genes related to ECM remodeling including *MMP1* and *MMP3* (Fig 5b, c). Matrix metalloproteinases MMP1 and MMP3 have been well-known early responders to tissue injury, actively regulating the inflammatory phase of healing by degradation of the ECM, stimulating leukocyte infiltration for resolution of inflammation and transition to the proliferative phase [47]. Cluster 4 exhibited overexpression of *POSTN* and *ASPN* (Fig. 5c) that are associated with ECM signaling, adhesion and migration. POSTN (Periostin) is a ligand for alpha-V/beta-3 and alpha-V/beta-5 integrins and supports adhesion and migration of epithelial cells [48], and has been shown to play a regulatory role in fibroblast proliferation and inflammation [49, 50]. ASPN (Asporin) is an ECM protein that has been found to inhibit TLR2- and TLR4-induced NF-κB activity and pro-inflammatory cytokine expression in macrophages [51]. TLR4 mediated inflammation drives the synergistic effect of hypoxia and hyperglycemia on impairment of diabetic wound healing [52], hence overexpression of *ASPN* might be an important determining factor for healing of DFUs. In a recent study, a distinct *ASPN* and *POSTN* enriched cluster of fibroblasts was described as mesenchymal and shown to have a more reticular dermis localization [45]. These subclusters (3,4,6 and 13) were also enriched with genes like *IL6, CHI3L1, PLA2G2A* and

TIMP1, commonly associated with an inflammatory signature (Fig. 5b, c, supplementary table 5). Based on our analysis, we identified a healing associated fibroblast signature consisting of ECM remodeling and inflammatory response related genes: *MMP1, MMP3, IL6, CHI3L1, ASPN, POSTN, PLA2G2A*.

Further analysis of these fibroblasts revealed that *IL6/TIMP1/PLA2G2A* and *CHI3L1* transcripts were detected simultaneously in ~38% of the cells suggestive of a common regulatory mechanism in HE-Fibro. We also noticed that 99.8% of *CHIL3L1* expressing cells exhibited significant expression of at least one of the ECM remodeling genes including *MMP1*, *MMP3*, *MMP11*, indicating a role of these genes in tissue repair. Based on these preliminary results we posit that CHIL3L1 is one of the key players in driving the healing phenotype of HE-Fibro by expressing proinflammatory and ECM genes together to improve wound repair. Several lines of evidence have previously implicated *CHI3L1* in dampening of chronic inflammation [53] , promoting M1 macrophage activation [54] and stimulating fibroblast proliferation [55] and ECM remodeling [56]. DEGs analysis on these DFU-Healers vs. other fibroblast clusters revealed some ubiquitous markers (*HIF1A, TNFAIP6*) that are overexpressed in HE-Fibro cells (Fig 5).

Pathway analysis indicated the activation of multiple immune and inflammatory pathways including IL6, HIF1A and ILK signaling in the fibroblasts from DFU-Healers (Fig. 5d). Moreover, upstream regulator genes like *TNF*, *HIF1A*, and *IL6,* were activated (Fig. 5e) in the DFU-Healers. HIF1A (Hypoxia-inducible factor 1-alpha) is a master-regulator that activates multiple factors to enhance wound healing by promoting cellular motility and proliferation, angiogenesis, re-epithelialization, and cell survival [57]. HIF1A also upregulates IL6 expression by binding to its promoter region [58], thereby promoting inflammation and cell proliferation.
Another notable gene in the molecular interaction network is TNF (Fig 5e), a potent proinflammatory cytokine that has been previously implicated in the wound healing process [59], and is known to be elevated shortly after wounding. TNF has also been shown to upregulate the expression MMP1 and MMP3 in human dermal fibroblasts via NFκB/p65 activation [60].

Deciphering communication among Healing associated Fibroblasts

Further, to determine possible communication among heterogeneous healing associated Fibroblasts (HE-Fibro subclusters 3,4, 6 and 13), we performed ligand, receptor and target gene co-expression analysis using the NicheNetR algorithm [13]. NicheNet predicts which ligands from one or more cell population(s), termed ‘sender/niche’, will most likely affect gene expression in interacting cell population(s), termed as ‘receiver/target’. Also, this algorithm can predict which specific target genes in the “receiver” cell populations are affected by the predicted ligands in the “sender” cell population(s). Subcluster 3 of the HE-Fibro with enrichment of both inflammatory and ECM remodeling genes (i.e., *IL-6,*

CHI3L1, MMP1) was selected as 'sender' cell population, while the remaining HE-Fibro subclusters (4, 6, 13) ('healers' fibroblasts) were treated as receiver cells. To filter out non-specific ligand and receptors, we also included control fibroblast sub-clusters (0,2,5), enriched in healthy non-DM and diabetic without DFU patients, as receiver cells. The analysis identified multiple ligands including IL6, CCL2 and TIMP1 with high correlation between differential expression of ligands in 'sender' fibroblasts and their target genes in the 'healer' fibroblasts (subclusters 4,6 and 13) but not in the 'control' fibroblasts (subclusters 0,2 and 5) (Fig. 5f) This indicates that fibroblasts from subcluster 3 are primarily interacting with other three subclusters of HE-Fibro subset enriched in DFU-healers rather than the 'control' fibroblasts subset enriched in healthy non-DM and diabetic with no-DFU patients. FN1 was enriched in all the HE-Fibro subclusters (3,4,6 and 13), while IL6, MMP13, CCL2, PTGS2 and VEGFA were enriched in only HE-Fibro subcluster 3 (Supplementary material 6). A heatmap displaying the connection between these key ligands that are expressed by HE-Fibro subcluster 3 (rows) and marker genes for the other HE-Fibro sub-clusters (4, 6, and 13) (columns) is shown in Fig 5g. For example, CCL2 overexpression in the 'receiver' HE-Fibro sub-clusters can be strongly predicted by the presence of IL6 in the 'sender' HE-Fibro sub-cluster, indicating possible molecular interaction between them. The circos plot shows association between ligands from "sender" cells, subcluster 3 (lower hemi-circle), and DEGs in receiver subclusters 4,6 and 13 (upper hemicircle) (Fig. 5h). The analysis identified IL6, MMP13, CCL2, CXCL12, CTGF, TIMP1 and VEGFA as key regulatory ligands in the HE-Fibro subcluster 3, altering the expression of downstream target genes in the HE-Fibro subcluster 4, 6 and 13. These identified ligands and their downstream targets might be responsible for the healing associated phenotype of HE-Fibro.

Based on enrichment and specific regulatory interaction among HE-Fibro subclusters in DFU-Healers, we postulate that their role consists of creating a beneficial physiological environment for accelerated DFU healing.

Spatial transcriptomics and immunohistochemistry further elucidate gene expression patterns in healing and non-healing DFUs

We subsequently selected well defined surgically excised DFU sections from healers and non-healers for additional characterization. They both displayed blood vessel proliferation and chronic inflammatory cell infiltrates predominantly with perivascular distribution (Fig. 6a,c). We stained for inflammatory fibroblast markers CHI3L1 and TIMP1 together with pan-fibroblast marker fibroblast activation protein (FAP) and discovered elevated numbers of triple positive cells within the ulcer area of healing DFUs, with the cells forming dense aggregates (Fig. 6d). However, in the non-healing ulcers these cells were far fewer and scarcely distributed (Fig. 6b). We also evaluated gene expression using a spatial transcriptomics approach. The GeoMx® platform enables spatial, high-plex quantitation of gene expression in tissue through the use of in-situ hybridization (ISH) probes that

target mRNA in tissue; attached to the probes are photocleavable and indexed oligonucleotides than can be liberated via UV light and counted with an Illumina® sequencer. Regions of interest (ROIs) were chosen after staining for immune cell marker CD45, vasculature marker aSMA and epithelial marker pan-Cytokeratin along with nuclear counter stain DAPI, to represent areas within the ulcer, at the edge of ulcer and adjacent non-injured tissue (Fig. 6a, c and Supplementary Fig S5a, b). Hierarchical clustering analysis of representative healing and non-healing specimens revealed dissimilar gene expression profiles according to location within the sample: ROIs at similar dermal depth grouped together. (Fig. 6e, f). The non-healing ulcer ROI was particularly distinct from neighboring ROIs (Fig. 6e), while the healing ulcer ROIs appeared more transcriptionally similar (Fig. 6f). Focusing on the ulcer localized ROIs, DE analysis from two healers (9 ROIs in total) and two non-healers (4 ROIs in total) showed 148 genes upregulated in healers and 57 in non-healers (Fig. 6g and Supplementary Fig S5c-f for additional DFUs). Among the most notable ones, HE-Fibro marker *PLA2G2A* and M1 macrophage marker *FOS* were overexpressed in healers (Fig. 6h, i), while M2 macrophage markers *TYMP* and *ANXA1* were upregulated in non-healers (Fig. 6j,k). Finally, gene ontology (GO) enrichment analysis unveiled cellular response to TNF as top biological function activated in healing ulcers and myeloid leukocyte migration in non-healing (Fig. 6l). Taken together, these findings verify our previous observations at the protein level and specify the location and functional roles of cell types reported in our scRNASeq dataset.

To further validate the finding based on spatial profiling that HE-Fibro mainly form niches in the wound bed to promote wound healing, we performed scRNA-seq analysis on multiple samples from the same patient. scRNA-Seq analysis was performed on skin specimens of the same patient from three different sites: wound bed, wound edge, and non-wound excess skin from a pressure sore excision (Supplementary Fig S4, supplementary material 7). The unsupervised analysis and cellular annotation revealed that HE-Fibro were enriched in the wound bed, but not in the wound edge and non-wounded samples (Supplementary Fig S4a, b). This unique wound bed enriched cell cluster exhibited significantly higher expression of HE-Fibro associated genes like *IL6*, *TNFAIP6*, *MMP1* and *CHI3L1* (Supplementary Fig. S4c). The absence of any other fibroblast cluster for the wound bed sample suggests that HE-Fibro originate from “normal” fibroblasts. These results further affirm an association of HE-Fibro with the wound healing process in an additional type of chronic wound and points toward heterogeneity of fibroblasts across different regions of ulcers.

Induced overexpression of CHI3L1 in dermal fibroblasts influences cell behavior

To explore the effects of inflammatory marker genes expression *in vitro*, we selected one of the top enriched genes *CHI3L1* and generated dermal fibroblast cell lines transduced

with lentiviral vectors overexpressing *CHI3L1* (CHI3L1-OE) or a control sequence (CTRL). Western blotting demonstrated a complete lack of expression in untreated cells and RT-qPCR analyses confirmed a significant upregulation of CHI3L1 with construct 2 (Supplementary Fig S5 a,b), which we selected for further experiments. In adhesion assays, more CHI3L1-OE cells attached to fibronectin coated surfaces compared to CTRL (Fig S5c,d), while diminished migration was observed in scratch wound experiments (Fig S5e,f). Altogether, these findings shed light on the potential functional roles of the HE-Fibro, indicating that they possess enhanced adherent and decreased migratory capacities and suggest that they are firmly anchored on the ECM and mediate healing through secretion of molecules.

Discussion:

In this study we performed large-scale unbiased scRNASeq to accurately and systematically profile patients with healing and non-healing DFUs, together with healthy non-DM subjects, and DM patients without DFUs, as controls. For a subset of patients, we also characterized forearm biopsies and PBMCs to evaluate any potential systemic effects of DM in presence of DFUs. To the best of our knowledge, we were the first groups to employ this approach in DFU samples [8], and we have now substantially expanded the number of cells sequenced, and incorporated state-of-the-art techniques like spatial transcriptomics, in order to gain novel insights into the transcriptomic landscape of DFU healing.

We identified a hitherto unreported fibroblast cell type associated with healing and expressing multiple immune and ECM remodeling related genes. We then corroborated the results at the protein level and with the additional sequencing modality of spatial transcriptomics, demonstrating their localization within the ulcer area. It has become increasingly apparent that dermal fibroblasts are a diverse and highly heterogeneous population with different functional roles in wound healing [61-65]. Fibroblasts at sites of inflammation, for instance within tertiary lymphoid structures, have been shown to acquire immune cell features [66], while in murine wounds' granulation tissue, a large proportion of fibroblasts is of myeloid cell origin [67]. A number of studies have also emphasized the interactions between fibroblasts and monocytes or macrophages in the context of inflammation and wound healing, implying a reciprocal relationship [68-70]. Our data suggest that specific fibroblast subtypes are key players in healing of DFUs and targeting them could be a therapeutic option.

Mapping the immune landscape of healers and non-healers revealed the presence of more M1 macrophages in healers and M2 in non-healers, as well as higher numbers of naïve and central memory T-cells, as opposed to more NK and NKT cells in non-healers. Impairment in the recruitment of macrophages and neutrophils in DFUs was recently demonstrated [71]. A dysregulation in the differentiation of peripheral blood derived T-

cells and diminished T-cell receptor repertoire diversity has been previously reported for DFU patients [72]. The majority of T-lymphocytes in our study originated from the blood samples, while macrophages were mostly located at the foot. Interestingly, in PBMCs of healers, inflammation pathways were mostly inhibited. These findings underline fundamental differences between systemic inflammation and the local wound inflammatory milieu. Overall, our results provide further evidence to support the claim that localized activated inflammatory response is required to surmount the chronic inflammation in DFUs, and progress to the next phases of wound healing [73, 74], while, conversely, inhibition of inflammatory processes at the systemic level appears beneficial for healing.

In summary, we present a comprehensive characterization of the DFU biosystem and report novel cell types and interactions. Our dataset will be a valuable resource for diabetes, dermatology, and wound healing research, and can serve as the baseline for designing *in vitro* and *in vivo* experiments for the assessment of therapeutic interventions focusing on one or more cell types. Future studies utilizing pre-enrichment via flow or magnetic cell sorting could further characterize specific populations and lead to the discovery of rare cells.

Author contributions VH, AV and MB obtained funding. HCH, VH, AV and MB supervised the project. GT, AV and MB designed the experiments. GT, BET, DS, SSB, TSS, RFS, IM, PW and AL conducted the experiments. GT, BET, DS, WJRP, BD, WP, AK, IV, SSB, AV and MB analyzed data. GT, BET, DS, SSB, WJRP, AV and MB wrote the manuscript.

Acknowledgments This work was supported by the NIDDK-sponsored Diabetic Complications Consortium grant 5U24DK115255-04 (AV and MB). AV received funding from the National Rongxiang Xu Foundation. GT received a George and Marie Vergottis Foundation Postdoctoral Fellowship award.

References:

1. Jeffcoate, W.J., et al., *Current Challenges and Opportunities in the Prevention and Management of Diabetic Foot Ulcers.* Diabetes Care, 2018. **41**(4): p. 645-652.
2. Armstrong, D.G., et al., *Five year mortality and direct costs of care for people with diabetic foot complications are comparable to cancer.* J Foot Ankle Res, 2020. **13**(1): p. 16.
3. Sen, C.K., *Human Wounds and Its Burden: An Updated Compendium of Estimates.* Adv Wound Care (New Rochelle), 2019. **8**(2): p. 39-48.
4. Baltzis, D., I. Eleftheriadou, and A. Veves, *Pathogenesis and treatment of impaired wound healing in diabetes mellitus: new insights.* Adv Ther, 2014. **31**(8): p. 817-36.
5. Armstrong, D.G., A.J.M. Boulton, and S.A. Bus, *Diabetic Foot Ulcers and Their Recurrence.* N Engl J Med, 2017. **376**(24): p. 2367-2375.
6. Stubbington, M.J.T., et al., *Single-cell transcriptomics to explore the immune system in health and disease.* Science, 2017. **358**(6359): p. 58-63.
7. Regev, A., et al., *The Human Cell Atlas.* Elife, 2017. **6**.
8. Theocharidis, G., et al., *Integrated Skin Transcriptomics and Serum Multiplex Assays Reveal Novel Mechanisms of Wound Healing in Diabetic Foot Ulcers.* Diabetes, 2020. **69**(10): p. 2157-2169.
9. Merritt, C.R., et al., *Multiplex digital spatial profiling of proteins and RNA in fixed tissue.* Nat Biotechnol, 2020. **38**(5): p. 586-599.
10. Tan, Y.S. and Y.L. Lei, *Isolation of Tumor-Infiltrating Lymphocytes by Ficoll-Paque Density Gradient Centrifugation.* Methods Mol Biol, 2019. **1960**: p. 93-99.
11. Butler, A., et al., *Integrating single-cell transcriptomic data across different conditions, technologies, and species.* Nat Biotechnol, 2018. **36**(5): p. 411-420.
12. Maaten, L.J.P.v.d. and G.E. Hinton, *Visualizing High-Dimensional Data Using t-SNE.* Journal of Machine Learning Research, 2008: p. 2579-2605.
13. Browaeys, R., W. Saelens, and Y. Saeys, *NicheNet: modeling intercellular communication by linking ligands to target genes.* Nat Methods, 2020. **17**(2): p. 159-162.
14. Magoc, T. and S.L. Salzberg, *FLASH: fast length adjustment of short reads to improve genome assemblies.* Bioinformatics, 2011. **27**(21): p. 2957-63.
15. Langmead, B. and S.L. Salzberg, *Fast gapped-read alignment with Bowtie 2.* Nat Methods, 2012. **9**(4): p. 357-9.
16. Reynolds, G., et al., *Developmental cell programs are co-opted in inflammatory skin disease.* Science, 2021. **371**(6527): p. eaba6500.
17. He, H., et al., *Single-cell transcriptome analysis of human skin identifies novel fibroblast subpopulation and enrichment of immune subsets in atopic dermatitis.* J Allergy Clin Immunol, 2020. **145**(6): p. 1615-1628.
18. Stoeckius, M., et al., *Simultaneous epitope and transcriptome measurement in single cells.* Nat Methods, 2017. **14**(9): p. 865-868.
19. Dumin, J.A., et al., *Pro-collagenase-1 (matrix metalloproteinase-1) binds the alpha(2)beta(1) integrin upon release from keratinocytes migrating on type I collagen.* J Biol Chem, 2001. **276**(31): p. 29368-74.
20. Arase, H., et al., *Cutting edge: the mouse NK cell-associated antigen recognized by DX5 monoclonal antibody is CD49b (alpha 2 integrin, very late antigen-2).* J Immunol, 2001. **167**(3): p. 1141-4.
21. Gagliani, N., et al., *Coexpression of CD49b and LAG-3 identifies human and mouse T regulatory type 1 cells.* Nat Med, 2013. **19**(6): p. 739-46.
22. Kazakova, M.H. and V.S. Sarafian, *YKL-40--a novel biomarker in clinical practice?* Folia Med (Plovdiv), 2009. **51**(1): p. 5-14.

23. Sanggaard, K.W., et al., *The TSG-6 and I alpha I interaction promotes a transesterification cleaving the protein-glycosaminoglycan-protein (PGP) cross-link.* J Biol Chem, 2005. **280**(12): p. 11936-42.
24. Milner, C.M. and A.J. Day, *TSG-6: a multifunctional protein associated with inflammation.* J Cell Sci, 2003. **116**(Pt 10): p. 1863-73.
25. Burgy, O. and M. Konigshoff, *The WNT signaling pathways in wound healing and fibrosis.* Matrix Biol, 2018. **68-69**: p. 67-80.
26. Whyte, J.L., et al., *Augmenting endogenous Wnt signaling improves skin wound healing.* PLoS One, 2013. **8**(10): p. e76883.
27. Vallee, A., et al., *Interactions between TGF-beta1, canonical WNT/beta-catenin pathway and PPAR gamma in radiation-induced fibrosis.* Oncotarget, 2017. **8**(52): p. 90579-90604.
28. Vela-Romera, A., et al., *Characterization of the human ridged and non-ridged skin: a comprehensive histological, histochemical and immunohistochemical analysis.* Histochem Cell Biol, 2019. **151**(1): p. 57-73.
29. Zhang, X., M. Yin, and L.J. Zhang, *Keratin 6, 16 and 17-Critical Barrier Alarmin Molecules in Skin Wounds and Psoriasis.* Cells, 2019. **8**(8).
30. Kerkhoff, C., et al., *Novel insights into the role of S100A8/A9 in skin biology.* Exp Dermatol, 2012. **21**(11): p. 822-6.
31. Kursar, M., et al., *Differential requirements for the chemokine receptor CCR7 in T cell activation during Listeria monocytogenes infection.* J Exp Med, 2005. **201**(9): p. 1447-57.
32. Hendriks, J., et al., *CD27 is required for generation and long-term maintenance of T cell immunity.* Nat Immunol, 2000. **1**(5): p. 433-40.
33. Mahnke, Y.D., et al., *The who's who of T-cell differentiation: human memory T-cell subsets.* Eur J Immunol, 2013. **43**(11): p. 2797-809.
34. Zeglinski, M.R. and D.J. Granville, *Granzymes in cardiovascular injury and disease.* Cell Signal, 2020. **76**: p. 109804.
35. Filen, J.J., et al., *Quantitative proteomics reveals GIMAP family proteins 1 and 4 to be differentially regulated during human T helper cell differentiation.* Mol Cell Proteomics, 2009. **8**(1): p. 32-44.
36. Bekeschus, S., et al., *Distinct cytokine and chemokine patterns in chronic diabetic ulcers and acute wounds.* Exp Dermatol, 2017. **26**(2): p. 145-147.
37. Spivia, W., et al., *Complement protein C1q promotes macrophage anti-inflammatory M2-like polarization during the clearance of atherogenic lipoproteins.* Inflamm Res, 2014. **63**(10): p. 885-93.
38. Mendes, K.L., D.F. Lelis, and S.H.S. Santos, *Nuclear sirtuins and inflammatory signaling pathways.* Cytokine Growth Factor Rev, 2017. **38**: p. 98-105.
39. Advedissian, T., et al., *E-cadherin dynamics is regulated by galectin-7 at epithelial cell surface.* Sci Rep, 2017. **7**(1): p. 17086.
40. Janson, D.G., et al., *Different gene expression patterns in human papillary and reticular fibroblasts.* J Invest Dermatol, 2012. **132**(11): p. 2565-72.
41. Korosec, A., et al., *Lineage Identity and Location within the Dermis Determine the Function of Papillary and Reticular Fibroblasts in Human Skin.* J Invest Dermatol, 2019. **139**(2): p. 342-351.
42. Haydont, V., et al., *Genome-wide profiling of adult human papillary and reticular fibroblasts identifies ACAN, Col XI alpha1, and PSG1 as general biomarkers of dermis ageing, and KANK4 as an exemplary effector of papillary fibroblast ageing, related to contractility.* Mech Ageing Dev, 2019. **177**: p. 157-181.
43. Nauroy, P., et al., *Human Dermal Fibroblast Subpopulations Display Distinct Gene Signatures Related to Cell Behaviors and Matrisome.* J Invest Dermatol, 2017. **137**(8): p. 1787-1789.
44. Ascension, A.M., et al., *Human Dermal Fibroblast Subpopulations Are Conserved across Single-Cell RNA Sequencing Studies.* J Invest Dermatol, 2020.

45. Sole-Boldo, L., et al., *Single-cell transcriptomes of the human skin reveal age-related loss of fibroblast priming.* Commun Biol, 2020. **3**(1): p. 188.
46. Tabib, T., et al., *SFRP2/DPP4 and FMO1/LSP1 Define Major Fibroblast Populations in Human Skin.* J Invest Dermatol, 2018. **138**(4): p. 802-810.
47. Dobaczewski, M., C. Gonzalez-Quesada, and N.G. Frangogiannis, *The extracellular matrix as a modulator of the inflammatory and reparative response following myocardial infarction.* J Mol Cell Cardiol, 2010. **48**(3): p. 504-11.
48. Gillan, L., et al., *Periostin secreted by epithelial ovarian carcinoma is a ligand for alpha(V)beta(3) and alpha(V)beta(5) integrins and promotes cell motility.* Cancer Res, 2002. **62**(18): p. 5358-64.
49. Yoshihara, T., et al., *Periostin plays a critical role in the cell cycle in lung fibroblasts.* Respir Res, 2020. **21**(1): p. 38.
50. Izuhara, K., et al., *Periostin in inflammation and allergy.* Cell Mol Life Sci, 2017. **74**(23): p. 4293-4303.
51. Yamaba, S., et al., *PLAP-1/Asporin Regulates TLR2- and TLR4-induced Inflammatory Responses.* J Dent Res, 2015. **94**(12): p. 1706-14.
52. Portou, M.J., et al., *Hyperglycaemia and Ischaemia Impair Wound Healing via Toll-like Receptor 4 Pathway Activation in vitro and in an Experimental Murine Model.* Eur J Vasc Endovasc Surg, 2020. **59**(1): p. 117-127.
53. Wang, R., et al., *Inflammatory-sensitive CHI3L1 protects nucleus pulposus via AKT3 signaling during intervertebral disc degeneration.* FASEB J, 2020. **34**(3): p. 3554-3569.
54. Zhao, T., et al., *Chitinase-3 like-protein-1 function and its role in diseases.* Signal Transduct Target Ther, 2020. **5**(1): p. 201.
55. Zhou, Y., et al., *Chitinase 3-like 1 suppresses injury and promotes fibroproliferative responses in Mammalian lung fibrosis.* Sci Transl Med, 2014. **6**(240): p. 240ra76.
56. Deutschmann, C., D. Roggenbuck, and P. Schierack, *The loss of tolerance to CHI3L1 - A putative role in inflammatory bowel disease?* Clin Immunol, 2019. **199**: p. 12-17.
57. Dallas, A., et al., *Acceleration of Diabetic Wound Healing with PHD2- and miR-210-Targeting Oligonucleotides.* Tissue Eng Part A, 2019. **25**(1-2): p. 44-54.
58. Niu, X., et al., *Hypoxia regulates angeogenic-osteogenic coupling process via up-regulating IL-6 and IL-8 in human osteoblastic cells through hypoxia-inducible factor-1alpha pathway.* Cytokine, 2019. **113**: p. 117-127.
59. Barrientos, S., et al., *Growth factors and cytokines in wound healing.* Wound Repair Regen, 2008. **16**(5): p. 585-601.
60. Lu, Y.E. and Y.J. Chen, *Resveratrol inhibits matrix metalloproteinase-1 and -3 expression by suppressing of p300/NFkappaB acetylation in TNF-alpha-treated human dermal fibroblasts.* Chem Biol Interact, 2021. **337**: p. 109395.
61. Driskell, R.R., et al., *Distinct fibroblast lineages determine dermal architecture in skin development and repair.* Nature, 2013. **504**(7479): p. 277-281.
62. Guerrero-Juarez, C.F., et al., *Single-cell analysis reveals fibroblast heterogeneity and myeloid-derived adipocyte progenitors in murine skin wounds.* Nat Commun, 2019. **10**(1): p. 650.
63. Lynch, M.D. and F.M. Watt, *Fibroblast heterogeneity: implications for human disease.* J Clin Invest, 2018. **128**(1): p. 26-35.
64. Mascharak, S., H.E. desJardins-Park, and M.T. Longaker, *Fibroblast Heterogeneity in Wound Healing: Hurdles to Clinical Translation.* Trends Mol Med, 2020. **26**(12): p. 1101-1106.
65. Philippeos, C., et al., *Spatial and Single-Cell Transcriptional Profiling Identifies Functionally Distinct Human Dermal Fibroblast Subpopulations.* J Invest Dermatol, 2018. **138**(4): p. 811-825.
66. Nayar, S., et al., *Immunofibroblasts are pivotal drivers of tertiary lymphoid structure formation and local pathology.* Proc Natl Acad Sci U S A, 2019. **116**(27): p. 13490-13497.

67. Sinha, M., et al., *Direct conversion of injury-site myeloid cells to fibroblast-like cells of granulation tissue.* Nat Commun, 2018. **9**(1): p. 936.
68. Donlin, L.T., et al., *Modulation of TNF-induced macrophage polarization by synovial fibroblasts.* J Immunol, 2014. **193**(5): p. 2373-83.
69. Humeres, C., et al., *Cardiac fibroblast cytokine profiles induced by proinflammatory or profibrotic stimuli promote monocyte recruitment and modulate macrophage M1/M2 balance in vitro.* J Mol Cell Cardiol, 2016.
70. Ploeger, D.T., et al., *Cell plasticity in wound healing: paracrine factors of M1/ M2 polarized macrophages influence the phenotypical state of dermal fibroblasts.* Cell Commun Signal, 2013. **11**(1): p. 29.
71. Sawaya, A.P., et al., *Deregulated immune cell recruitment orchestrated by FOXM1 impairs human diabetic wound healing.* Nat Commun, 2020. **11**(1): p. 4678.
72. Moura, J., et al., *Impaired T-cell differentiation in diabetic foot ulceration.* Cell Mol Immunol, 2017. **14**(9): p. 758-769.
73. Stone, R.C., et al., *A bioengineered living cell construct activates an acute wound healing response in venous leg ulcers.* Sci Transl Med, 2017. **9**(371).
74. Tellechea, A., et al., *Topical Application of a Mast Cell Stabilizer Improves Impaired Diabetic Wound Healing.* J Invest Dermatol, 2020. **140**(4): p. 901-911 e11.

Figures:

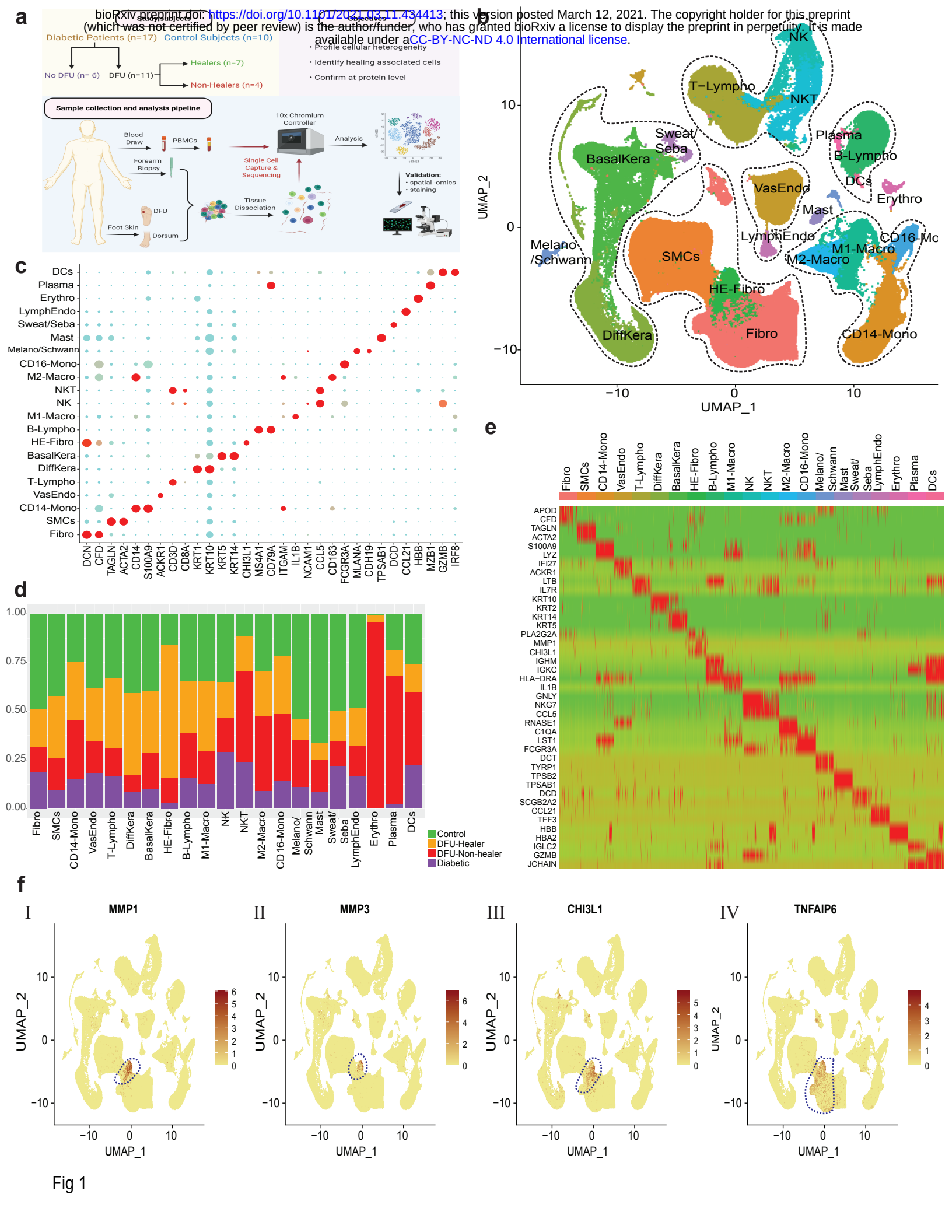

Fig 1

Figure 1. ***Single-cell RNA sequencing mediated identification and characterization of unique healing enriched fibroblasts in Diabetic Foot Ulcers (DFUs)***
(a) Schematic overview of the study design and number of samples per clinical group. **(b)** Uniform Manifold Approximation and Projection (UMAP) embedding of the entire dataset consisting of 174,962 cells. The cells are colored by orthogonally generated clusters, and labeled by manual cell type annotation (HE-Fibro: Healing Enriched Fibroblasts, Fibro: Fibroblasts, SMCs: Smooth Muscle Cells, BasalKera: Basal Keratinocytes, DiffKera: Differentiated Keratinocytes, Sweat/Seba: Sweat and Sebaceous gland cells; Melano/Schwann: Melanocytes and Schwann cells; Mast: Mast cells; VasEndo: Vascular Endothelial cells; LymphEndo: Lymphatic Endothelial cells; CD14-Mono: CD14+ Monocytes, CD16-Mono: CD16+ Monocytes, M1-Macro: M1 Macrophages, M2-Macro: M2 Macrophages, Erythro: Erythrocytes, NK: Natural Killer cells, T-Lympho: T-Lymphocytes, NKT: NK cells and T lymphocytes; B-Lympho: B-Lymphocytes, Plasma: Plasma cells, DCs: Dendritic Cells). **(c)** Dot plot showing expression of different cell type specific marker genes, used to annotate the cell types. Size of dots indicates percentage of cells in each cell cluster expressing the marker gene; color represents averaged scaled expression levels; cyan: low, red: high. **(d)** Stacked bar plots showing the proportion of different cell types across the 4 clinical groups. Green: Healthy subjects, Orange: DFU-Healers, Red: DFU-Non-healers, PurpleDiabetic patients. **(e)** Heatmap showing the top highly expressed (red) genes in each of the cell clusters. **(f)** Feature plots depicting the expression of key genes *(I) MMP1*, *(II) MMP3*, *(III) CHI3L1*, *(IV) TNFAIP6*, that were significantly overexpressed in the healing enriched fibroblasts associated with healing of DFUs.

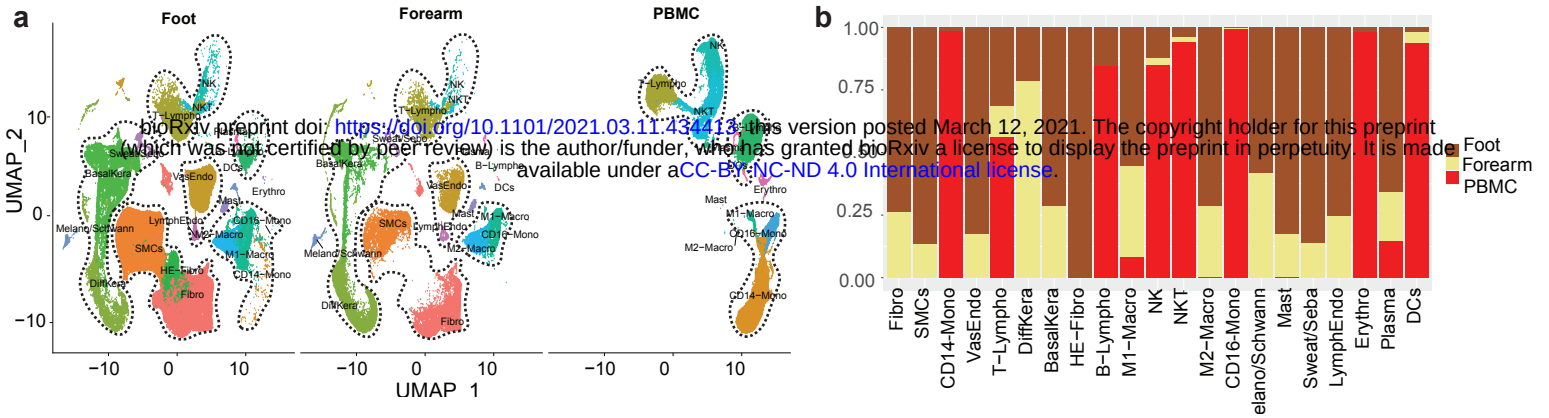

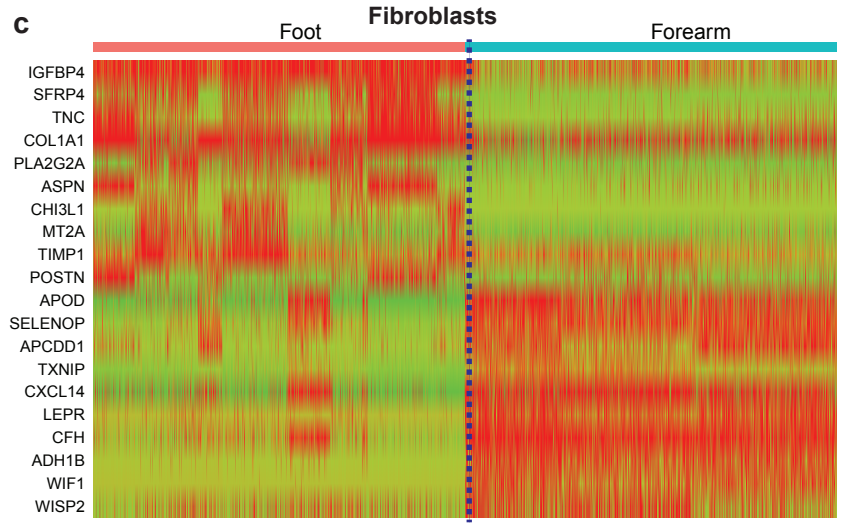

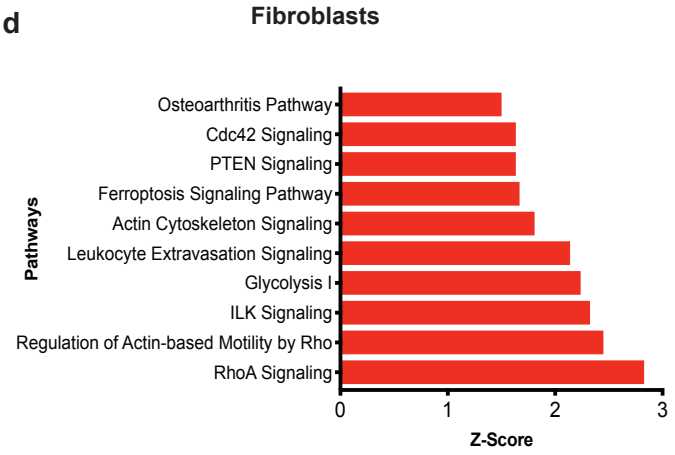

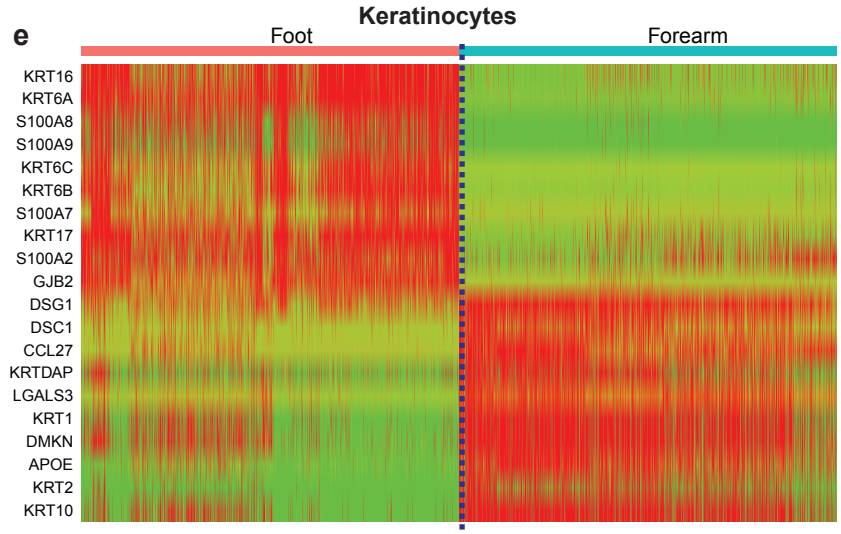

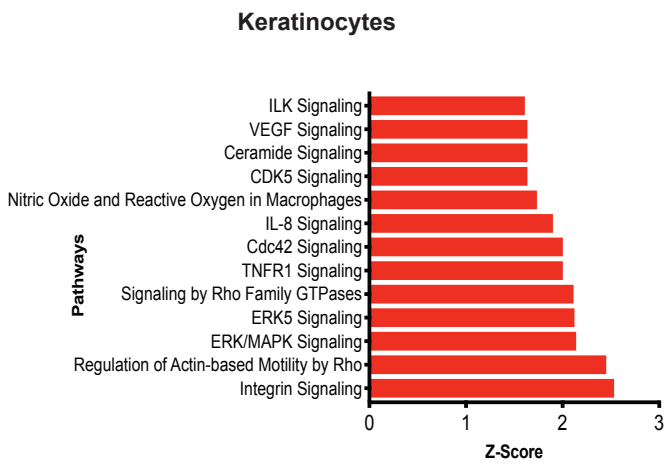

Fig 2

Figure 2. ***Comparative single cell transcriptome analysis profiles of foot, forearm, and PBMCs, delineating gene signatures and biological pathways across anatomical sites***. **(a)** Split UMAP of Foot, Forearm, and PBMC samples. The cell clusters were annotated manually according to various canonical and novel cell types based on expression of specific markers (as described in Fig. 1b). **(b)** Stacked bar plots showing the proportion (y-axis) of different cell type from Foot, Forearm, and PBMC. Dark brown: Foot, Beige: Forearm, Red: PBMCs. **(c)** Heatmap showing significantly differentially expressed genes between foot and forearm fibroblast cell clusters. Relative gene expression is shown in pseudo color, where green represents down regulation, and red represents up regulation. **(d)** Pathway enrichment analysis on genes that are significantly differentially expressed between foot and forearm cell fibroblast clusters. The pathways analysis was performed using Ingenuity Pathways analysis (IPA) tool that calculate significance of impact on pathways using one-tailed Fisher's exact test and Z-score. The pathways with P value <.01 and Z score >2 were considered significantly activated. **(e)** Heatmap showing significantly differentially expressed genes in keratinocytes cell clusters between foot and forearm samples. **(f)** Pathway enrichment analysis on genes that are significantly differentially expressed between foot and forearm keratinocytes cell clusters.

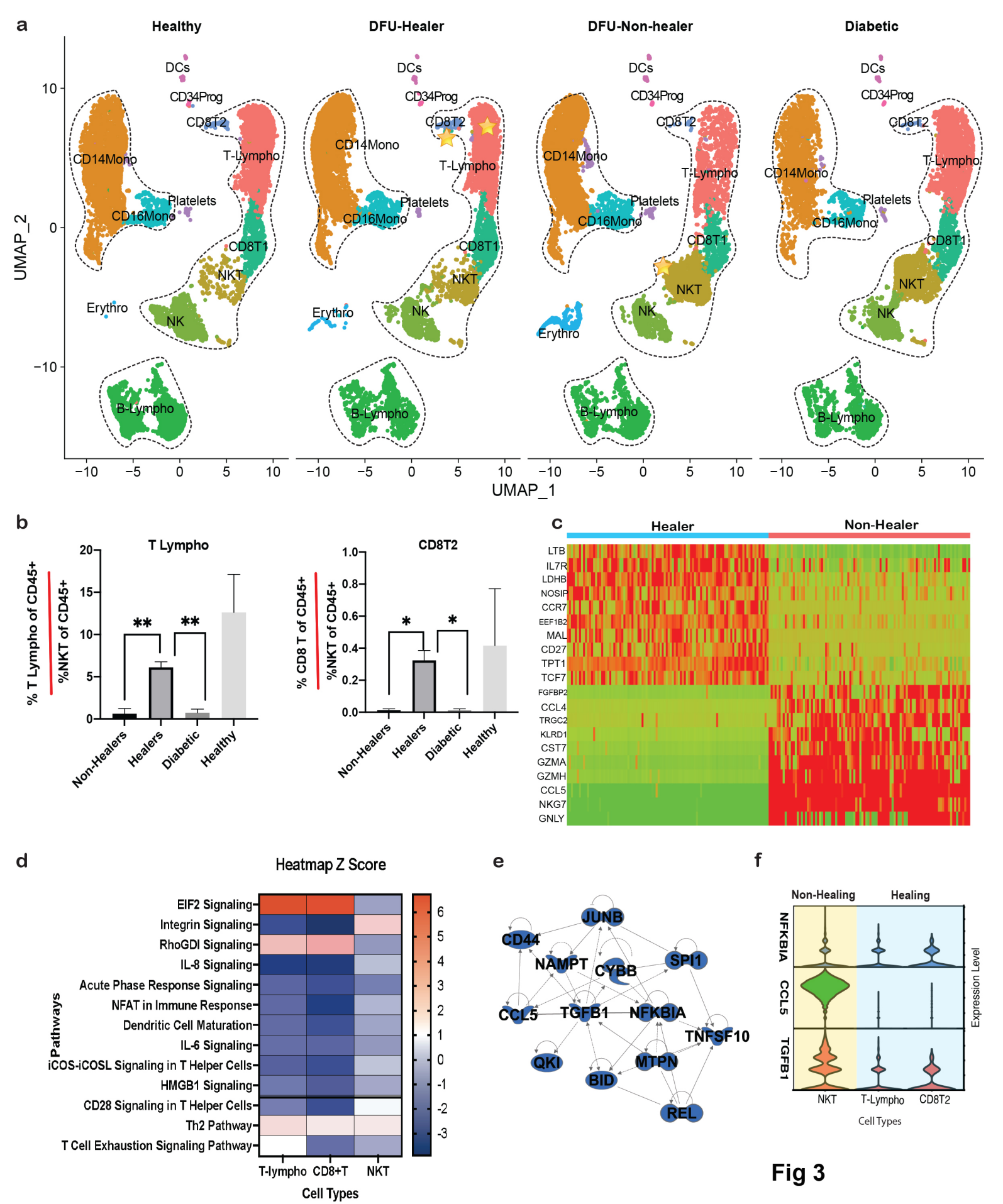
a
Healthy
DFU-Healer
DFU-Non-healer
Diabetic
DCs
CD34Prog
CD8T2
CD14Mono
T-Lympho
Platelets
CD16Mono
CD8T1
NKT
Erythro
NK
B-Lympho
UMAP_2
UMAP_1
b
T Lympho
% T Lympho of CD45+
%NKT of CD45+
CD8T2
% CD8 T of CD45+
Non-Healers
Healers
Diabetic
Healthy
c
Healer
Non-Healer
LTB
IL7R
LDHB
NOSIP
CCR7
EEF1B2
MAL
CD27
TPT1
TCF7
FGFBP2
CCL4
TRGC2
KLRD1
CST7
GZMA
GZMH
CCL5
NKG7
GNLY
d
Heatmap Z Score
EIF2 Signaling
Integrin Signaling
RhoGDI Signaling
IL-8 Signaling
Acute Phase Response Signaling
NFAT in Immune Response
Dendritic Cell Maturation
IL-6 Signaling
iCOS-iCOSL Signaling in T Helper Cells
HMGB1 Signaling
CD28 Signaling in T Helper Cells
Th2 Pathway
T Cell Exhaustion Signaling Pathway
Pathways
T-lympho
CD8+T
NKT
Cell Types
e
JUNB
CD44
NAMPT
CYBB
SPI1
CCL5
TGFB1
NFKBIA
TNFSF10
QKI
MTPN
BID
REL
f
Non-Healing
Healing
NFKBIA
CCL5
TGFB1
Expression Level
NKT
T-Lympho
CD8T2
Cell Types

Fig 3

Figure 3. ***Comparative transcriptome profiles analysis of PBMCs in different clinical groups, uncovering differences in systemic immune landscape associated with wound healing response in DFUs. (a)*** UMAP dimensionality reduction embedding of PBMCs from DFU-Healers, DFU Non-healers, Healthy subjects, and non-DFU DM patients. The identified cell types were DCs: dendritic cells; VasEndo: vascular endothelial cells; T-lympho: T lymphocytes; CD8T1: $CD8^+$ T lymphocytes cluster 1; CD8T2: $CD8^+$ T lymphocytes cluster 2; NK: natural killer cells; NKT: natural killer and T cells; B-lympho: B lymphocytes; CD14Mono: $CD14^+$ monocytes; CD16Mono: $CD16^+$ monocytes **(b)** Bar plots showing percentage of T-lymphocyte (T-lympho) and $CD8^+$ T cell cluster 2 (CD8T2) per percentage of NKT cells in the $CD45^+$ subset of cells across various clinical groups. DFU-healers depict significantly higher ratio of T-lympho and CDT2 cell cluster in comparison to DFU-Non-healers and Diabetic. Bars were plotted with standard error of the mean (SEM). *P* value was calculated by Welch's *t*-test. *Pvalue <.05, **Pvalue<.01 **(c)** Heatmap showing significant DEGs in healers compared to Non-healers in the T-lympho, CD8T2 and NKT cell clusters. **(d)** Biological pathways that are significantly (P value <.01) activated (Z score >1.5) /inhibited (Z score <-1.5) in T-lympho, CD8T2 cells of healers in contrast to NKT cells of non-healers. Activation and inhibition of key upstream regulators is shown in pseudo color, where blue represents inhibition, and red represents activation. **(e)** Upstream regulatory molecules significantly inhibited (blue) in the T-lympho and CD8T2 cells of healers as compared to non-healers at systemic level. **(f)** Violin plots showing expression levels of 3 key upstream regulator molecules- *NFKBIA, CCL5,* and *TGFB1*, in the NKT, T-Lympho, and CD8T2 clusters.

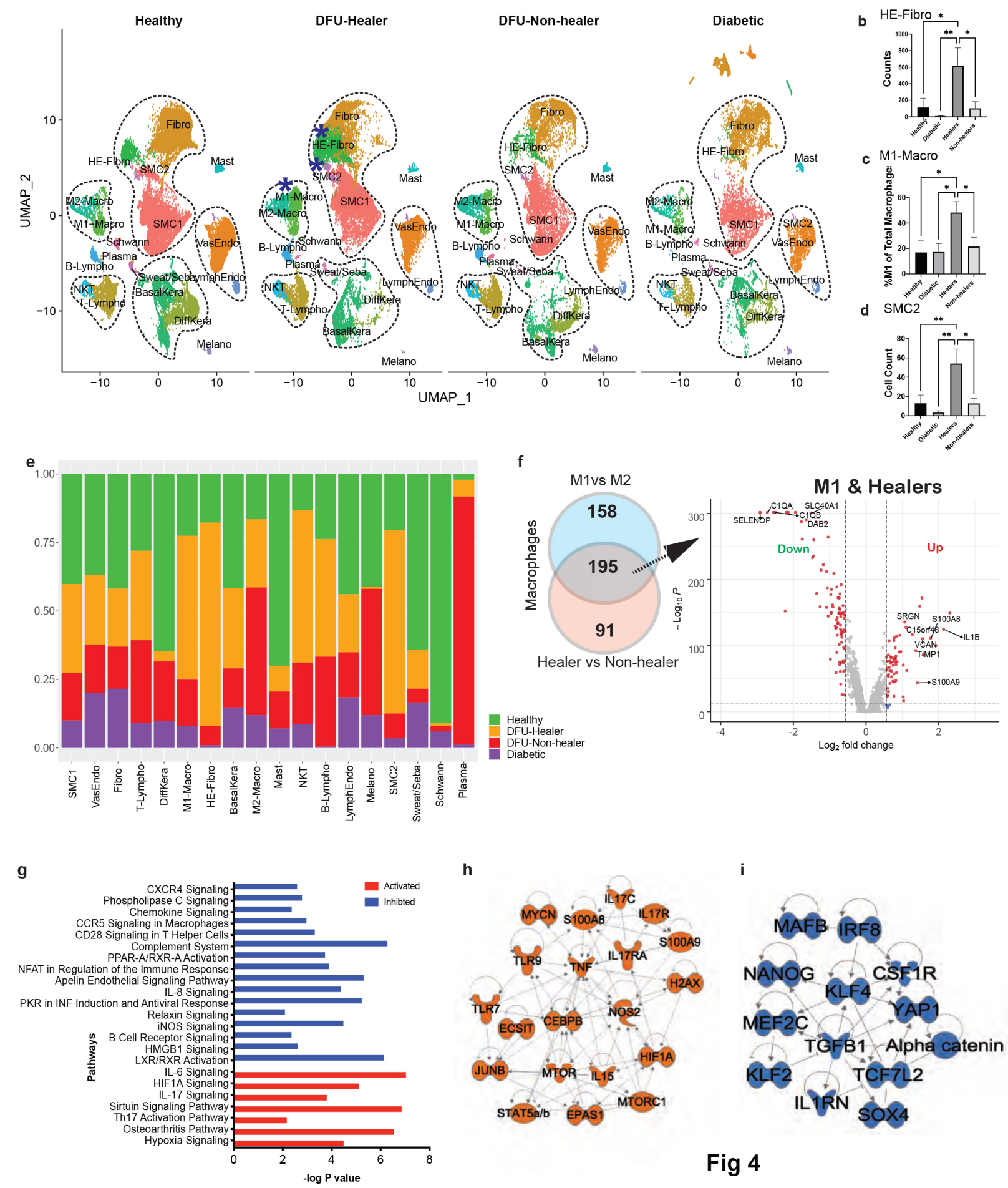
Healthy
DFU-Healer
DFU-Non-healer
Diabetic
UMAP_1
UMAP_2
Fibro
HE-Fibro
SMC2
SMC1
Mast
M2-Macro
M1-Macro
Schwann
VasEndo
Plasma
B-Lympho
Sweat/Seba
LymphEndo
NKT
T-Lympho
BasalKera
DiffKera
Melano
b
HE-Fibro
Counts
c
M1-Macro
%M1 of Total Macrophages
d
SMC2
Cell Count
Healthy
Diabetic
Healers
Non-healers
e
Healthy
DFU-Healer
DFU-Non-healer
Diabetic
f
M1vs M2
158
195
91
Macrophages
Healer vs Non-healer
M1 & Healers
Down
Up
C1QA
SLC40A1
C1QB
SELENOP
DAB2
SRGN
S100A8
C15orf48
IL1B
VCAN
TIMP1
S100A9
Log2 fold change
g
Activated
Inhibited
CXCR4 Signaling
Phospholipase C Signaling
Chemokine Signaling
CCR5 Signaling in Macrophages
CD28 Signaling in T Helper Cells
Complement System
PPAR-A/RXR-A Activation
NFAT in Regulation of the Immune Response
Apelin Endothelial Signaling Pathway
IL-8 Signaling
PKR in INF Induction and Antiviral Response
Relaxin Signaling
iNOS Signaling
B Cell Receptor Signaling
HMGB1 Signaling
LXR/RXR Activation
IL-6 Signaling
HIF1A Signaling
IL-17 Signaling
Sirtuin Signaling Pathway
Th17 Activation Pathway
Osteoarthritis Pathway
Hypoxia Signaling
Pathways
-log P value
h
IL17C
MYCN
S100A8
IL17R
S100A9
TLR9
TNF
IL17RA
H2AX
TLR7
ECSIT
CEBPB
NOS2
HIF1A
JUNB
MTOR
IL15
MTORC1
STAT5a/b
EPAS1
i
MAFB
IRF8
NANOG
CSF1R
KLF4
YAP1
MEF2C
TGFB1
Alpha catenin
KLF2
TCF7L2
IL1RN
SOX4

Fig 4

Figure 4. ***Comparative analysis of transcriptome profiles of foot samples in the different clinical groups, elucidating differences in cell type composition, gene expression and biological pathways.*** **(a)** UMAP dimensionality reduction embedding of foot cells from DFU-Healers, DFU-Non-healers, Healthy subjects, and non-DFU DM patients. The cellular clusters depicting significant enrichment in the healers are marked with blue asterisks. Comparative analysis depicted **(b)** HE-Fibro, **(c)** M1 Macrophages and **(d)** SMC2 cellular enrichment in the foot sample from DFU healers. Results are expressed using bar graphs representing the mean and SEM values in the groups (*p-value < 0.05, ** p-value < 0.01 by One way ANOVA with Fisher's LSD *post hoc* test). **(e)** Stacked bar plots showing the proportions of different cell types across the different clinical groups (Green: Healthy subjects, Orange: DFU-Healers, Red: DFU-Non-healers, Purple: non-DFU DM patients). **(f)** Venn diagram analysis to compare genes that are differentially expressed between M1 and M2 Macrophages and macrophages between healers vs. non-healers. The comparison identified 195 genes that are differently expressed in M1 macrophages from the healers. Volcano plot showing the genes that are significantly differential expressed (red dots) in M1 macrophages of healers (Benjamini Hochberg corrected P-value <0.00001, FC>1). **(g)** Selected biological pathways that are significantly (P value <0.01) effected in the healing associated M1 macrophages. Each bar represents a pathway with significance of enrichment determined using the one tail Fisher's Exact t-test (-log10 P.value is shown on primary X-axis). The directionality of each pathway is depicted using a pseudocolor (red for activated, blue for inhibited). Regulators that are significantly **(h)** activated and **(i)** inhibited in the M1 macrophages from the healers. The activation and inhibition of pathways was measured based on Z-score calculation using IPA analysis platform.

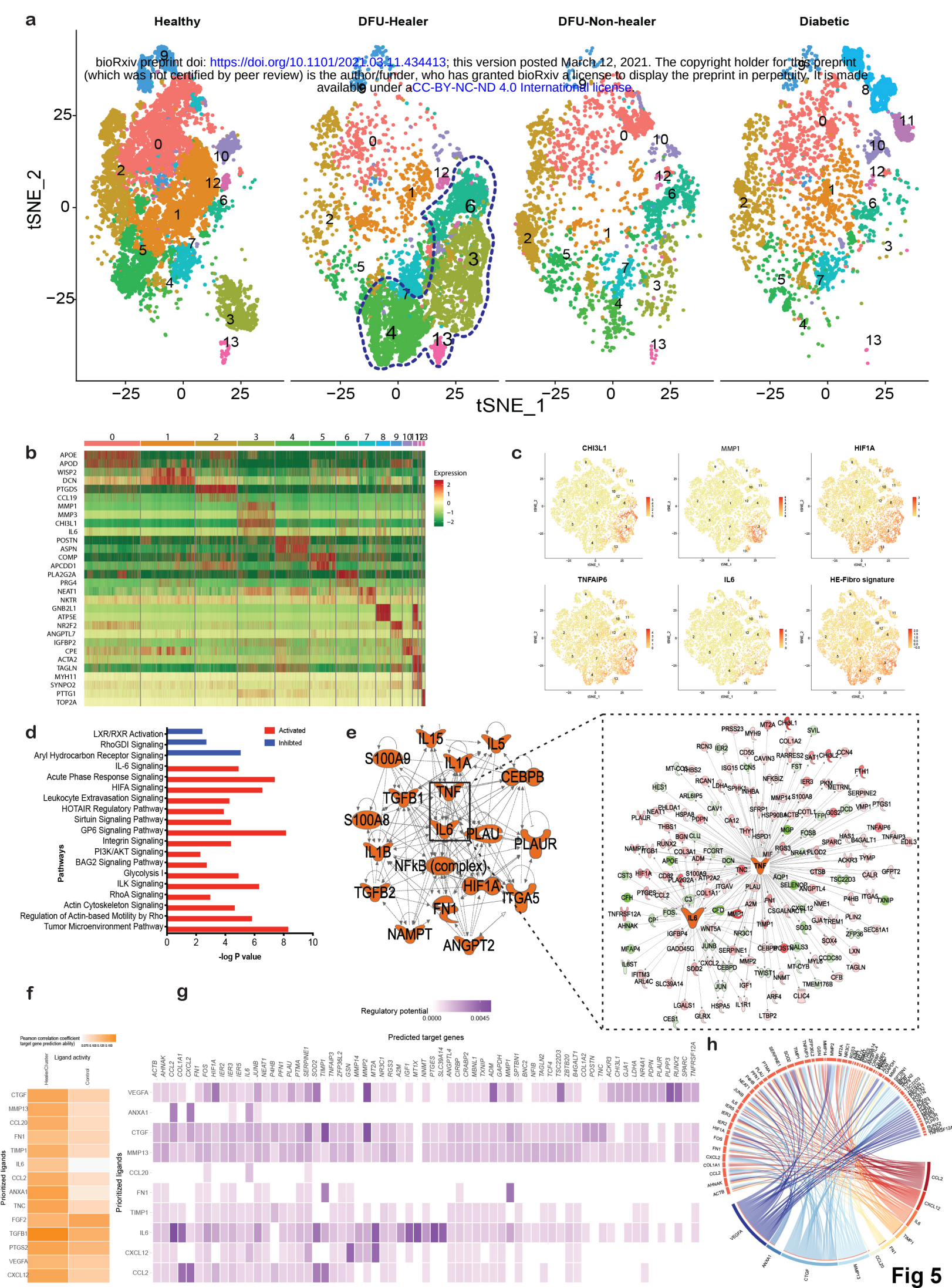

Figure 5. Identification and characterization of *distinct subpopulations of fibroblasts with specific gene signature associated with healing DFUs*. (a) t-distributed Stochastic Neighbor Embedding (t-SNE) analysis depicting 14 sub-clusters of fibroblasts. The subclusters enriched in DFU-Healers are marked with lasso. **(b)** Heatmap showing the top highly expressed genes (red) in subclusters. **(c)** Feature plots depicting the expression of key genes *(MMP1, CHI3L1,* HIF1A, *IL6*, *TNFAIP6*) and HE-Fibro signature (*MMP1, MMP3, IL6, CHI3L1, ASPN, POSTN, PLA2G2A*) across healing associated fibroblast subclusters. (d) Selected biological pathways that are significantly (P value <0.01) affected in the healing enriched fibroblasts. The directionality of each pathway is depicted using a pseudo color (red for activated, blue for inhibited). (e) Regulators that are significantly activated in the healing enriched fibroblasts. The detailed map of two key activators IL6 and TNF along with target genes is also shown. (**f**) Heatmap showing the Pearson correlation between ligands from 'sender' subcluster 3 and target gene expression in 'healer fibroblasts, i.e., the other HE-Fibro subclusters 4,6,13 (left column), and 'control' fibroblasts sub-cluster 0,2,5 (right column). A darker orange color indicates a higher Pearson correlation between the ligand and gene expression within the receiver cell population. **(g)** This heatmap of select ligands expressed by HE-Fibro subcluster 3 (rows) to regulate the genes which are differentially expressed by the 'healer' fibroblasts (columns). Well established ligand-target gene interactions shown with a darker shade of purple. **(h)** Circos plot displaying the association between ligands expressed in the subcluster 3 (bottom semi-circle) with their interactive differentially expressed genes in the subcluster 4,6 and 13.

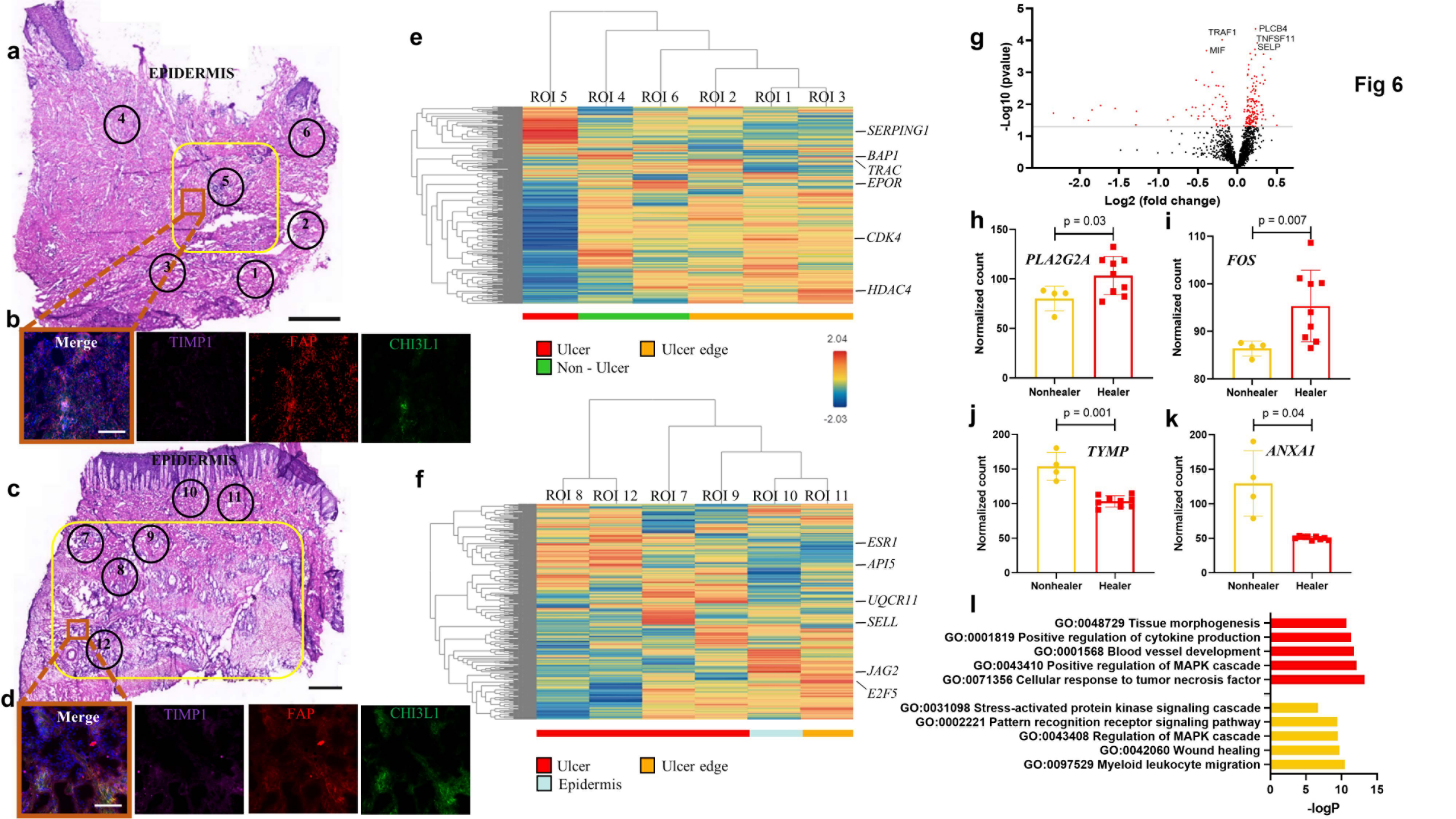
a
EPIDERMIS
4
6
5
2
3
1
b
Merge
TIMP1
FAP
CHI3L1
c
EPIDERMIS
10
11
7
9
8
12
d
Merge
TIMP1
FAP
CHI3L1
e
ROI 5
ROI 4
ROI 6
ROI 2
ROI 1
ROI 3
SERPING1
BAP1
TRAC
EPOR
CDK4
HDAC4
Ulcer
Ulcer edge
Non - Ulcer
2.04
-2.03
f
ROI 8
ROI 12
ROI 7
ROI 9
ROI 10
ROI 11
ESR1
API5
UQCR11
SELL
JAG2
E2F5
Ulcer
Ulcer edge
Epidermis
g
TRAF1
PLCB4
TNFSF11
SELP
MIF
-Log10 (pvalue)
Log2 (fold change)
h
p = 0.03
PLA2G2A
Normalized count
Nonhealer
Healer
i
p = 0.007
FOS
Normalized count
Nonhealer
Healer
j
p = 0.001
TYMP
Normalized count
Nonhealer
Healer
k
p = 0.04
ANXA1
Normalized count
Nonhealer
Healer
l
GO:0048729 Tissue morphogenesis
GO:0001819 Positive regulation of cytokine production
GO:0001568 Blood vessel development
GO:0043410 Positive regulation of MAPK cascade
GO:0071356 Cellular response to tumor necrosis factor
GO:0031098 Stress-activated protein kinase signaling cascade
GO:0002221 Pattern recognition receptor signaling pathway
GO:0043408 Regulation of MAPK cascade
GO:0042060 Wound healing
GO:0097529 Myeloid leukocyte migration
-logP

Fig 6

Figure 6. Exploring the spatial transcriptome of DFU-Healers and DFU-Non-healers. **(a, c)** Representative H&E-stained sections from a non-healing (a) and a healing (c) DFU. Yellow box demarcates the ulcer area and numbered circles the ROIs selected for sequencing. (**b, d**) Immunofluorescence staining for HE-Fibro markers TIMP1 (pink), CHI3L1 (green) and pan-fibroblast marker FAP (red) performed on a serial section from the same sample. DAPI was used for nuclear counterstain. The location of the image capture is noted with an orange box on (a) and (c). (**e, f**) Hierarchical clustering analysis heatmaps depict the transcriptomic profiles of the selected ROIs. The most highly expressed gene per ROI is highlighted. ROIs were annotated based on their location as Ulcer (red), Non-Ulcer (green), Ulcer edge (orange) and Epidermis (light blue). Expression levels are shown according to the gradient middle right (blue low to red high). (**g**) Volcano plot showing DE analysis results from ROIs within the ulcer in Healers (N=2 patients, 9 ROIs) vs Nonhealers (N=2 patients, 4 ROIs). Each dot represents a gene, with red ones being above the significance threshold. The top five genes are highlighted. (**h-k**) Selected notable genes upregulated in Healers (h,i) and Nonhealers (j,k). (**l**) GO analysis for biological processes enriched in Healers (top, red) and Nonhealers (bottom, yellow). Scale bars are 1 mm in (a,c) and 100 μm in (b,d).